Lab on a Chip

Devices and applications at the micro- and nanoscale

Accepted Manuscript

Volume 17
Number 1
7 January 2017
Pages 1-200

Lab on a Chip

Devices and applications at the micro- and nanoscale

rsc.li/loc

ISSN 1473-0197

ROYAL SOCIETY OF CHEMISTRY

PAPER
Chengzhi Hu, Bradley J. Nelson et al.
Characterization of size-dependent mechanical properties of
top-growing cells using a lab-on-a-chip device

ROYAL SOCIETY OF CHEMISTRY

rsc.li/loc

Journal Name

ARTICLE TYPE

Acoustofluidics 24: Theory and experimental measurements of acoustic interaction force

Shahrokh Sepehrirahnama[†a], Abhishek Ray Mohapatra[c], Sebastian Oberst[†a,b], Yan Kei Chiang[b,a], David A. Powell[b], and Kian-Meng Lim[c]

The motion of small objects in acoustophoresis depends on the acoustic radiation force and torque. These are nonlinear phenomena originating from wave scattering, and consist of primary and secondary components. The primary radiation force is the force acting on an object due to the incident field, in the absence of other objects. The secondary component, known as acoustic interaction force, accounts for the interaction among objects, and contributes to the clustering patterns of objects, as commonly observed in experiments. In this tutorial, the theory of acoustic interaction forces is presented using the force potential and Partial-Wave expansion approaches, and the distinguishing features of these forces such as rotational coupling and non-reciprocity are described. Theoretical results are compared to experimental measurements of interaction forces using a glass micro-capillary setup to explain the practical challenges. Finally, the phenomenon of clustering patterns induced by the close-range interaction of objects is demonstrated to point out the considerations about multiple collision and the predicted clustering patterns entirely due to the interaction force. Understanding the principles of acoustic interaction enables us to develop novel acoustofluidic applications beyond the typical processing of large populations of particles and with focus on the controlled manipulation of small clusters.

1 Introduction

In an acoustofluidic process, objects within a pressure field are manipulated according to the acoustic radiation force and torque fields, which depend on their scattering behaviour[1–3]. These forces and torques are mainly dependent on objects' dimensions, geometry, and the external acoustic field. They can be applied to change the dynamic balance of an object, which depends on other forces such as weight, buoyancy, and fluid drag. In particular, acoustic manipulation has been shown to be a promising technique for objects with size much smaller than the wavelength, commonly referred to as particles. In most practical applications, including ultrasonic manipulation of biological cells or functional micro-/nano-beads in microfluidic chips, a population of such particles in a host fluid is treated simultaneously, resulting in particle agglomeration. This clustering is associated with the pair-wise interaction between objects in a population, which is referred to as the acoustic interaction force or secondary radiation

force[4–12]. In this tutorial, we present the theory of the acoustic interaction force and related experimental techniques for its measurement using a microfluidic chip.

The primary radiation force is a nonlinear acoustic phenomenon, originating from the product of the external acoustic field and the scattered field of an object, as shown in Fig. 1(a), meaning that it does not include the scattered field of other particles and reflection from the walls of the fluid domain[2,13–15]. The secondary force, which is called acoustic interaction hereafter, is a form of nonlinear acoustic interaction and occurs when there are multiple objects in the acoustic field[4–8,10,15,16]. This force originates from the product of the pressure and velocity fields scattered from one object with those scattered from another (Fig. 1(b)). Similarly, the notion of acoustic interaction forces can be extended to an object and the walls of a fluid domain which, similarly to another object, reflects the acoustic wave. This physical description can be generalized to explain the primary force as an interaction between the target body and an object located at infinity, emitting acoustic energy. Despite the underlying physics of primary and interaction forces being the same, they exhibit different effects on objects in a sound field, with the primary force driving them towards acoustic traps (stable equilibrium locations), while the interaction force determines how they interact with each other during cluster formation.

[a] Centre for Audio, Acoustics and Vibration, University of Technology Sydney, Sydney, Australia

E-mail: shahrokh.sepehrirahnama@uts.edu.au; sebastian.oberst@uts.edu.au

[b] School of Engineering and Information Technology, University of New South Wales, Canberra, Australia

[c] Mechanical Engineering Department, National University of Singapore, Singapore 117575, Singapore

Both primary and interaction forces depend on material properties[2,17], shape[18], viscosity[19] and object size[20]. In addition, interaction forces decrease as the distances between a target and its neighbouring objects increase[5–7,15]. Hence, the acoustic interaction is considered as a close-range nonlinear effect of objects on each other[3,21–23]. The action of this acoustic interaction continues even after particles arrive at acoustic traps, where the primary force is negligible. Viscosity contributes to the primary and interaction forces by affecting the scattering process and consequently inducing acoustic streaming[13,24,25]. This hydrodynamic contribution mainly depends on the type of acoustic streaming flow, which can be determined from the scattering behaviour of the objects or the walls of the fluid domain, the viscosity level, and the relative difference in the material properties of the buffer fluid and the objects[13,19,26–28]. The streaming contribution to the primary force can vary from a fraction of its radiation component[13,19,26,27] to orders of magnitude larger[28], for sufficiently dense objects and when the viscous boundary layer is comparable to the object's size. In addition to the material density and the viscous layer, the relative distance between the objects is a major factor in determining the hydrodynamic contribution to the acoustic interaction.

Mutual interaction between oscillating particles was reported first in 1906 for pulsating bubbles in terms of the Bjerknes force[16,29–31]. The primary Bjerknes force acting on a single pulsating bubble arises from the reaction of the surrounding fluid to the radiated momentum of the outgoing wave due to the surface pulsation[16,30,31], which is the same physical principle behind the primary radiation force. The difference is that the primary Bjerknes force is associated with surface pulsation, stimulated either internally or externally, while the primary radiation force is due to the scattering of an external acoustic field. This implies that the primary radiation force also exists for acoustically rigid objects with zero surface-oscillation due to the effect of radiation pressure[2,13]. These forces are referred to as primary forces, since they are obtained under the assumption of a single object in a fluid domain[16,32]. Similarly, the secondary Bjerknes force corresponds to the interaction force, as both describe the interaction between a pair of objects, including gas bubbles and liquid droplets, with the dominant contribution coming from surface oscillations[31–36]. The interaction force is also applicable to solid objects, due to the contribution from radiation pressure[5–8,15].

The acoustic interaction force has been studied theoretically[4–6,8,15,37], numerically[7,11,21,38], and experimentally[9,10,12,37,39–41]. For a pair of objects, the acoustic interaction force has a component that acts in the centre-to-centre direction, inducing attraction or repulsion similar to electrostatic forces between charges. In addition, it can have a component in the tangential direction, which induces coupled rotational motion[7,15]. The acoustic interaction forces on a pair of identical objects are equal, and act in opposite directions, while they violate the action-reaction principle for non-identical pairs[15]. These properties of acoustic interaction result in different regimes of cluster formation and growth[23,41], compared to the typical dynamics of agglomeration under electrostatic interaction.

Agglomeration processes due to acoustic interaction forces have been observed in both microfluidic applications and for in-air levitation, cf. Fig. 1. The agglomeration patterns depend on the properties of the external acoustic field[10,42], cf. Fig. 1(c) and (e), the material properties of the buffer fluid and the objects under manipulation[43], cf. Fig. 1(d), and the number of particles[23], cf. Fig. 1(f). The average size of spherical particles in these applications varies from 10 μm to around 1 mm and the ultrasonic frequencies range from 45 kHz to 3 MHz, indicating the wide range of size and frequency at which the clustering is a significant part of the acoustic manipulation process. Particle clusters also exhibit collective mechanical properties that can be measured from the dynamic motion and deformation of the clusters, implying acoustic interaction forces can act as binding forces that give structural integrity to the cluster of particles[41].

Among various applications of the interaction force, biological cell patterning in tissue culture[42], seed particle technology[44–46] and single particle trapping or manipulation[47,48] are noteworthy examples. An accurate estimation of the agglomeration time and patterns of cell clusters in the vicinity of acoustic traps requires a better understanding of the role of acoustic interaction[42]. The interaction force acting on biological cells can be comparable to or orders of magnitude larger than the primary radiation force, particularly when cells are already within the ultrasonic trap and their relative distance is small enough to trigger a strong interaction, leading to novel ways of ultrasound manipulation of biological cells, e.g., isolation, sorting and assembly of small clusters[49]. In seed particle technology, as the size of particles approaches the nanometer-scale, the influence of the drag induced by acoustic streaming becomes stronger, compared with the primary radiation force[50]. With the use of preloaded micrometer-sized seed particles, the particle-particle interactions introduce significant interaction force, enabling agglomeration of sub-micron particles, even for a small number of them[44–46]. An example is the extraction of sperm cells from low concentration samples using small clusters of polystyrene beads to enhance their acoustic trapping[51,52]. Furthermore, studies of spherical particles and biological cells with size comparable to the acoustic wavelength show that the effects of interaction forces can be observed at locations where the primary force is close to zero and during the formation of clusters in the vicinity of the acoustic trap[47,48]. Therefore, accurate estimation of the interaction force is also important for single particle or cell manipulation. Recently, an acoustofluidic device was developed to assist in the study of chemical compositions of biological cells using Raman spectroscopy[53]. It operates with a resonance chamber and the contact-free levitation of particles, resulting in measurements with little noise, which are required to conduct accurate scans of a Raman spectrum. In these applications of acoustophoresis, the occurrence of clustering can be attributed to the patterns of acoustic interaction between the objects, which depend on their surrounding conditions too. The understanding of the interaction force is important to optimise the concentration of such particles and the input power for a stable configuration at the pressure node during scanning[53], and potentially novel ways of controlling such interactions can be developed for practical applications.
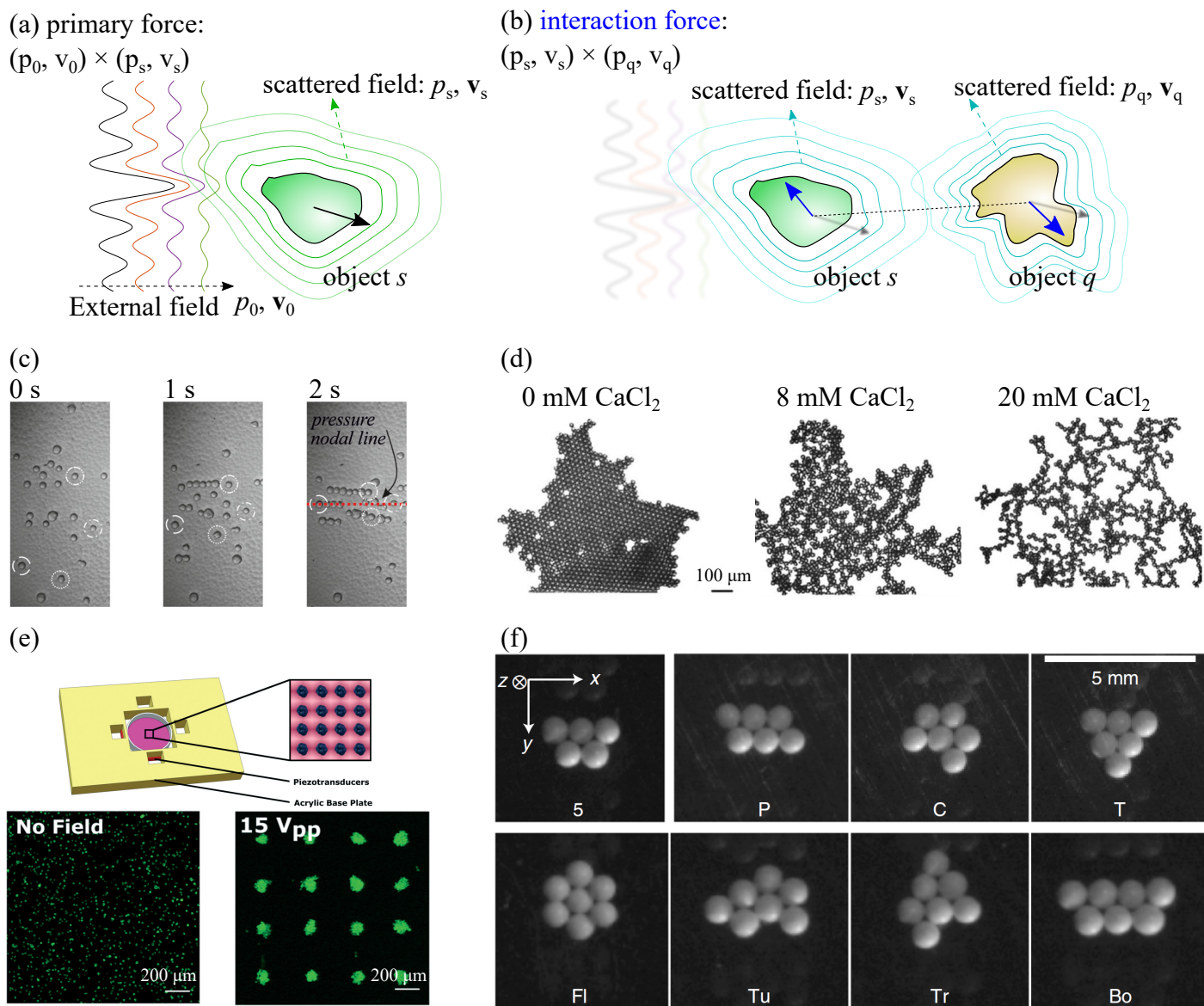
Fig. 1 Physical principle of (a) the primary radiation force, indicated by the black arrow acting on the centroid of object *s*, and (b) the acoustic interaction force, indicated by the blue arrow acting on the centroids of object *s* and *q*, as a result of the product of two distinct fields. Cluster formation due to close-range acoustic interaction between objects, (c) in a microfluidic cavity excited by a standing wave with Kisker PSI-10 spherical particles of $10\mu m$ diameter at a frequency of 1.481 MHz (Reprinted from Baasch, T., Leibacher, I. and Dual, J. Multibody dynamics in acoustophoresis, The Journal of the Acoustical Society of America 141 (3), pp 1664—1674. Copyright 2017, with permission from Acoustic Society of America, https://doi.org/10.1121/1.4977030), (d) $25\mu m$ Polystyrene particles in a 3 MHz ultrasound trap subject to various concentrations of electrolyte buffer (Reprinted from Bazou, D., Coakley, W. T., Meek, K. M., Yang, M. and Pham, D. T., Characterisation of the morphology of 2-D particle aggregates in different electrolyte concentrations in an ultrasound trap, Colloids and Surfaces A: Physicochemical and Engineering Aspects 243 (1—3), pp 97—104, Copyright (2004), with permission from Elsevier, https://doi.org/10.1016/j.colsurfa.2004.04.075), (e) schematic of membrane-stained C2C12 myoblast (ATCC) particles patterned as sixteen distinct clusters in a microfluidic cavity, using dual standing waves at 2.1 MHz, (Reprinted from Armstrong, J. P., Maynard, S. A., Pence, I. J., Franklin, A. C., Drinkwater, B. W., and Stevens, M. M. Spatio-temporal quantification of acoustic cell patterning using Voronoï tessellation. Lab on a Chip, 19(4), pp 562—573 (2019), under Creative Commons Attribution 3.0 Unported Licence https://doi.org/10.1039/C8LC01108G), and (f) various patterns for different numbers of levitated Polyethylene spheres (Cospheric) with diameter of $710 - 850\mu m$ in air at 45.65 kHz (Reprinted by permission from Springer Nature Customer Service Centre GmbH: Nature, Nature Physics Lim, M. X., Souslov, A., Vitelli, V., and Jaeger, H. M., Cluster formation by acoustic forces and active fluctuations in levitated granular matter, (2019), Nature Physics, 15(5), pp 460–464 https://doi.org/10.1038/s41567-019-0440-9).

2 Theoretical estimation of the interaction force

We start with a review of acoustic wave propagation and the theory of acoustic radiation force for an ideal fluid, i.e. a fluid where viscous effects can be neglected. Two analytical models of acoustic interaction force are discussed in detail. The first model, based on force potentials, is valid for small sub-wavelength particles, while the second model is based on Partial-Wave expansion and is applicable to particles of any size. A numerical model of acoustic

interaction force applicable to different shapes, sizes and material properties is discussed. Finally, using the theoretical models, important features of acoustic interaction force are described.

2.1 Fundamentals and governing equations

Ideal fluid flow is governed by the Navier-Stokes equations [13,54]:

$$\partial_t \overline{\rho} + \boldsymbol{\nabla}(\overline{\rho \mathbf{v}}) = 0,$$
$$\partial_t(\overline{\rho \mathbf{v}}) + \boldsymbol{\nabla} \cdot (\overline{\rho \mathbf{v} \mathbf{v}}) = -\boldsymbol{\nabla}\overline{p}, \qquad (1)$$

where $\overline{\rho}$, $\overline{p}$, $\overline{\mathbf{v}}$ denote the density, pressure and velocity fields, respectively, $\overline{\mathbf{v} \mathbf{v}}$ is the dyadic product of the velocity vectors, ∂_t denotes the time-dependent rate operator, and ∇ denotes the spatial gradient operator with respect to position vector $\mathbf{x}$ of a material point in the fluid domain. Derivation of the governing equations of acoustic wave propagation from Eq. (1) relies on the perturbation expansion of the density, pressure and velocity fields [2,54] up to the second-order approximation, as follows,

$$\overline{\rho} = \rho_f + \rho + \tilde{\rho} + \mathcal{O}(3),$$
$$\overline{p} = p_f + p + \tilde{p} + \mathcal{O}(3), \qquad (2)$$
$$\overline{\mathbf{v}} = \mathbf{v}_f + \mathbf{v} + \tilde{\mathbf{v}} + \mathcal{O}(3),$$

where ρ_f, p_f, and $\mathbf{v}_f$ are zero order density, pressure and velocity fields, respectively, associated with a steady-state fluid flow or a static fluid (time-independent), which are also referred to as the background flow fields. Without loss of generality, we can assume no background velocity field $\mathbf{v}_f = \mathbf{0}$ for the rest of the formulation [54]. The sum of neglected terms of order three and higher is denoted by $\mathcal{O}(3)$. The first and second order fields are denoted by $(\rho, p, \mathbf{v})$ and $(\tilde{\rho}, \tilde{p}, \tilde{\mathbf{v}})$, respectively.

2.1.1 Acoustic wave propagation

By substituting the first order fields into Eq. (1), the first order approximation of the nonlinear Navier-Stokes equations is derived as a linear set of equations,

$$\partial_t \rho = -\rho_f \boldsymbol{\nabla} \cdot \mathbf{v},$$
$$\rho_f \partial_t \mathbf{v} = -\boldsymbol{\nabla} p. \qquad (3)$$

From the equation of state of fluids, the relation between first order pressure and density fields becomes $p = c_f^2 \rho$, where c_f is the speed of sound in the fluid within the isentropic limit. This allows us to derive the governing equations of the acoustic wave propagation from Eq. (3) as

$$c_f^2 \nabla^2 p = \partial_{tt} p, \qquad (4)$$

where ∂_{tt} denotes second-order differentiation with respect to time t and $\nabla^2 = \boldsymbol{\nabla} \cdot \boldsymbol{\nabla}$ denotes the Laplacian operator. Furthermore, the first order terms ρ, p and $\mathbf{v}$ are commonly referred to as the acoustic density, pressure and velocity fields, respectively. The theory of acoustic interaction force in the non-viscous limit relies on Eq. (4) which describes the incident, scattered, reflected and refracted waves in an ideal fluid. The acoustic velocity can be

expressed as $\mathbf{v} = \boldsymbol{\nabla}\phi$, with ϕ denoting the scalar velocity potential field.

For an object q in the fluid domain, the acoustic pressure applied at the exterior surface causes the object to oscillate at the wave frequency, and this rigid-body oscillation is expressed as [5,13]

$$\rho_q \Omega_q \partial_t \mathbf{w}_q = -\int_{\Gamma_q} p \mathbf{n}_q d\Gamma, \qquad (5)$$

where ρ_q denotes the density of the object, Ω_q is the volume of the object enclosed by the exterior surface Γ_q with $\mathbf{n}_q$ being the outwards normal vector, and $\mathbf{w}_q$ denotes the velocity of the rigid-body oscillation. The time-averaged position of the object over one period of the wave remains the same, indicating the time-averaged action of the acoustic pressure is zero. Similarly, the oscillatory rotation of objects due to the acoustic pressure applied at their surface can be described using Newton's second law of motion; however, the time-averaged orientation of the object remains unchanged. The time-average of a time-dependent field $H(\mathbf{x}, t)$ over a cycle of an acoustic wave is

$$\langle H \rangle = \frac{1}{T} \int_0^T H dt, \qquad (6)$$

where T denotes the wave period.

2.1.2 Second-order effects of acoustic excitation

The time-average of a time-harmonic acoustic field $p(\mathbf{x}, t) = p(\mathbf{x})e^{-i\omega t}$ is zero, since $\langle e^{-i\omega t} \rangle = 0$. However, the time-averaged value of the product of two harmonic fields is non-zero, which implies a resultant action in a temporal frame much slower than that of the acoustic fields. Here, the time-averaged second-order approximation of the Navier-Stokes equations is presented to demonstrate the influence of such product terms, and describe their effects in terms of a second-order radiation pressure. By substituting Eq. (2) into (1), the time-averaged second-order approximation of the Navier-Stokes equations becomes [13,54]

$$\rho_f \boldsymbol{\nabla} \cdot \langle \tilde{\mathbf{v}} \rangle = m_b, \qquad m_b = -\boldsymbol{\nabla} \cdot \langle \rho \mathbf{v} \rangle$$
$$\boldsymbol{\nabla} \langle \tilde{p} \rangle = \mathbf{f}_b, \qquad \mathbf{f}_b = -\langle \rho \partial_t \mathbf{v} \rangle - \rho_f \langle (\mathbf{v} \cdot \boldsymbol{\nabla}) \mathbf{v} \rangle = -\boldsymbol{\nabla} \cdot \langle \mathbf{v} \mathbf{v} \rangle, \qquad (7)$$

where m_b and $\mathbf{f}_b$ are the volumetric mass and force source terms that are proportional to the product of acoustic density and velocity fields. For an ideal fluid, the second-order pressure $\langle \tilde{p} \rangle$ can be expressed using $\rho_f \partial_t \mathbf{v} = -\boldsymbol{\nabla} p$ from Eq. (3), $p = c_f^2 \rho$, and $(\mathbf{v} \cdot \boldsymbol{\nabla})\mathbf{v} = \frac{1}{2}\boldsymbol{\nabla} \cdot (v^2)$, in the common form [2,13,26,55] as

$$\langle \tilde{p} \rangle = \frac{1}{2}\kappa_f \langle p^2 \rangle - \frac{1}{2}\rho_f \langle v^2 \rangle, \qquad (8)$$

where $\kappa_f = 1/\rho_f c_f^2$ denotes the mean fluid compressibility, and $v^2 = \mathbf{v} \cdot \mathbf{v}$.

2.1.3 Acoustic radiation force and torque

In the ideal fluid limit, the viscous stresses become zero. The time-averaged force (up to second-order accuracy) applied to an object in the acoustic field is obtained directly from the fluid pres-

sure as

$$\mathbf{F} = \left\langle \int_{\Gamma(t)} (p+\tilde{p})\mathbf{n}d\Gamma \right\rangle = \left\langle \int_{\Gamma(t)} p\mathbf{n}d\Gamma \right\rangle + \int_{\Gamma} \langle \tilde{p} \rangle \mathbf{n}d\Gamma, \quad (9)$$

where $\Gamma(t)$ and Γ denote the instantaneous and at-rest surface of the object, respectively. The first term on the right-hand side of Eq. (9) can be simplified further using the divergence theorem and the first-order momentum conservation Eq. (3), as follows,

$$\left\langle \int_{\Gamma(t)} p\mathbf{n}d\Gamma \right\rangle = \left\langle \int_{\hat{\Gamma}} p\mathbf{n}d\Gamma \right\rangle - \left\langle \int_{\Omega(t)} \nabla p d\Omega \right\rangle,$$
$$= \int_{\hat{\Gamma}} \langle p \rangle \mathbf{n}d\Gamma + \left\langle \int_{\Omega(t)} \rho_f \partial_t \mathbf{v} d\Omega \right\rangle, \quad (10)$$

where $\hat{\Gamma}$ is a fixed surface surrounding the object and $\Omega(t)$ denotes the instantaneous volume bounded by the object's surface $\Gamma(t)$ and $\hat{\Gamma}$. The first term on the right-hand side of Eq. (10) is zero since $\langle p \rangle = 0$. By applying the material derivative operator $d/dt = \partial_t + \mathbf{v}\nabla$ to the second term on the second line of Eq. (10)[56], we obtain

$$\frac{d}{dt} \int_{\Omega(t)} \mathbf{v}d\Omega = \int_{\Omega(t)} \partial_t \mathbf{v}d\Omega - \int_{\Gamma(t)} \mathbf{v}(\mathbf{v}\cdot\mathbf{n})d\Gamma. \quad (11)$$

By substituting Eq. (11) into (10), using the divergence theorem, and considering $\langle d/dt \int_{\Omega(t)} \mathbf{v}d\Omega \rangle = \mathbf{0}$, the contribution to the force of the acoustic pressure acting on the surface of the object becomes

$$\left\langle \int_{\Gamma(t)} p\mathbf{n}d\Gamma \right\rangle = \left\langle \int_{\Gamma(t)} \rho_f \mathbf{v}\mathbf{v}\cdot\mathbf{n}d\Gamma \right\rangle = -\left\langle \int_{\Gamma(t)} \boldsymbol{\sigma}_{\text{Rey}} \cdot \mathbf{n}d\Gamma \right\rangle, \quad (12)$$

where $\boldsymbol{\sigma}_{\text{Rey}}$ denotes the Reynolds stresses that arise from low-amplitude oscillation of the surface of the object due to external wave excitation. The radiation stress tensor $\langle \boldsymbol{\sigma} \rangle$ is expressed as

$$\langle \boldsymbol{\sigma} \rangle = -\langle \tilde{p} \rangle \mathbf{I} + \langle \boldsymbol{\sigma}_{\text{Rey}} \rangle = -\left[\frac{1}{2}\kappa_f \langle p^2 \rangle - \frac{1}{2}\rho_f \langle v^2 \rangle \right] \mathbf{I} - \rho_f \langle \mathbf{v}\mathbf{v} \rangle, \quad (13)$$

where $\mathbf{I}$ denotes the second-order unitary tensor. Substituting Eqs. (8), (12) and (13) into Eq. (9) and using momentum conservation in (7), the force integral becomes

$$\mathbf{F} = \left\langle \int_{\Gamma(t)} \left(-\tilde{p}\mathbf{I} + \boldsymbol{\sigma}_{\text{Rey}} \right)\cdot\mathbf{n}d\Gamma \right\rangle$$

$$\mathbf{F} = \int_{\hat{\Gamma}} \langle -\tilde{p}\mathbf{I} + \boldsymbol{\sigma}_{\text{Rey}} \rangle \mathbf{n}d\Gamma + \left\langle \int_{\Omega(t)} (\nabla\tilde{p} + \nabla\cdot\mathbf{v}\mathbf{v})d\Omega \right\rangle \quad (14)$$

$$\mathbf{F} = \int_{\hat{\Gamma}} \langle -\tilde{p}\mathbf{I} + \mathbf{v}\mathbf{v} \rangle \mathbf{n}d\Gamma.$$

From (14), the radiation force $\mathbf{F}$ and, similarly radiation torque $\mathbf{T}$ acting on a object are obtained in terms of the radiation stresses, as follows,

$$\mathbf{F} = -\int_{\Gamma} \langle \boldsymbol{\sigma} \rangle \cdot \mathbf{n}d\Gamma, \qquad \mathbf{T} = -\int_{\Gamma} \mathbf{x} \times \left[\langle \boldsymbol{\sigma} \rangle \cdot \mathbf{n} \right]d\Gamma, \quad (15)$$

where $\mathbf{x}$ is the position vector with respect to a given origin e.g., the centre of mass of the object. The term Γ denotes any surface enclosing the object, i.e. at-rest exterior surface of the object or a fixed fictitious surface $\hat{\Gamma}$. Due to the conservation of radiated

momentum, this surface can take arbitrary shape and can be considered at any distance away, provided it encloses the object in an ideal fluid[2]. In the case of a single object in a viscous fluid, this integration surface needs to be separated from the object by several times the thickness of the viscous boundary layer. At such distances, viscous dissipation effects are negligible and the acoustic velocity field becomes irrotational[19].

2.2 Multiple scattering and acoustic interaction force

For a population of N objects in a external acoustic field, the total acoustic pressure satisfying the wave equation, Eq.(4), becomes

$$p = p_0 + \sum_{n=1}^{n=N} p_n, \quad (16)$$

where p_0 denotes the external pressure field, coming from a source outside of the fluid domain, and p_n is the partial scattered pressure from the nth object. The incident pressure $\hat{p}$ for object q is defined as

$$\hat{p}_q = p_0 + \sum_{\substack{n=1 \\ n \neq q}}^{N} p_n = p_0 + \sum_{n;q} p_n, \quad (17)$$

where $\sum_{n;q}$ is short-hand notation for the sum of scattering from the other $N-1$ objects, excluding target object q, and $p = \hat{p}_q + p_q$. Eq. (17) implies that the scattering from each object depends on the external pressure field and the scattered pressure of other objects. Therefore, in general, the total pressure field is obtained by solving the fully coupled multi-scattering problem, using computational methods, e.g., the Boundary Element (BE) or Finite Element (FE) methods for acoustic wave propagation. For the special case of spherical objects, the multiple scattering problem can be solved by using Partial-Wave expansion, also known as a multipole series expansion, which will be discussed in Section 2.4.

To revisit the definitions of the primary and interaction forces, the quadratic terms of the radiation stresses in Eq. (13) are expanded with respect to their external and scattered acoustic fields. Together with Eq. (17) for the target object q, we get

$$p^2 = \left(\hat{p}_q + p_q \right)\left(\hat{p}_q + p_q \right) = \hat{p}_q^2 + 2\hat{p}_q p_q + p_q^2$$
$$= p_0^2 + 2p_0 \sum_{n;q} p_n + \left(\sum_{n;q} p_n \right)^2 + 2\hat{p}_q p_q + p_q^2. \quad (18)$$

Similar expansions can be written for the $\hat{\mathbf{v}}\cdot\hat{\mathbf{v}}$ and $\hat{\mathbf{v}}\hat{\mathbf{v}}$ terms of the radiation stresses. Considering the radiation force and torque acting on object q, the terms p_0^2, $\hat{\mathbf{v}}_0 \cdot \hat{\mathbf{v}}_0$ and $\hat{\mathbf{v}}_0\hat{\mathbf{v}}_0$ due to the incident field produce no force[2,5,6,15]. The stresses induced by the self-product of scattered fields of the object, p_q^2, $\mathbf{v}_q \cdot \mathbf{v}_q$ and $\mathbf{v}_q\mathbf{v}_q$, produce forces and torques that are of the order of $(ka)^6$. For sub-wavelength objects in the Rayleigh limit $ka \ll 1$, this results in more than three orders of magnitude smaller forces compared to the primary and interaction forces; hence, these terms can be neglected[2]. A single isolated object only experiences the radiation stresses due to the cross terms such as $p_0 p_q$, which give rise to the primary radiation force[2]. This implies that the primary radiation force explicitly depends on the external pressure field p_0.
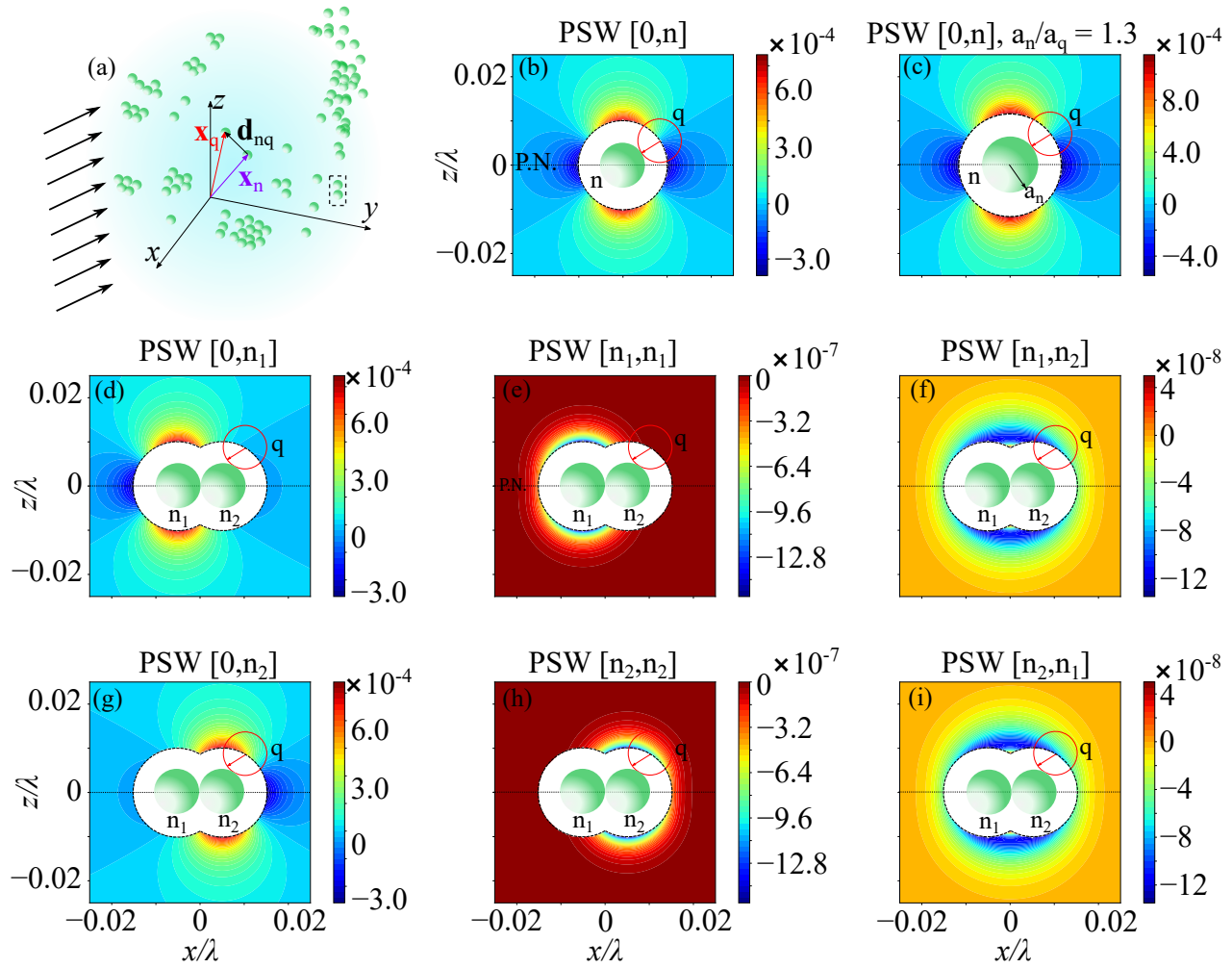
Fig. 2 (a) Spherical objects interacting under an external acoustic field. Large and small clusters are formed at various locations regardless of the existence of a global acoustic trap, typically a pressure or velocity node for plane standing waves (PSW). Panel (b) shows the interaction potential for a pair of identical spheres with the source n fixed and target q used for probing the potential. Panel (c) is the landscape of interaction potential for the case of the source sphere being around 2.2 times larger than the target. The case of three spheres is shown in (d) to (i). The presented numerical results were obtained for spherical polystyrene beads with $ka_n \approx 0.03$, in water with density ratio $\rho_n/\rho_f = 1.050$ and the ratio of the compressibility modulus $\kappa_n/\kappa_f = 0.388$, in the absence of viscous losses, viscous boundary layer, and viscosity-induced streaming. The Rayleigh index of $ka_n \approx 0.03$ corresponds to 5 μm polystyrene beads in water subject to an ultrasonic wave at 1.5 MHz. The pairs of indices indicate the partial interaction potential associated with pressure and velocity fields from the objects with the same labels, for instance $[0, n_1]$ corresponds to $\langle p_0 p_{n_1} \rangle$ and $\langle \mathbf{v}_0 \mathbf{v}_{n_1} \rangle$ in Eq. (28). Figure reprinted with permission from Sepehrirahnama S., Lim K.-M., Physical Review E, 102, 043307, 2020. Copyright (2020) by the American Physical Society, `https://doi.org/10.1103/PhysRevE.102.043307`

The remaining terms in the radiation stresses, corresponding to the second and fourth terms of the second line of Eq. (18), lead to the sum of the primary and interaction force[7,8,15], which can be further expanded as

$$\langle \boldsymbol{\sigma}_q \rangle = \langle \boldsymbol{\sigma}_0^{(q)} \rangle + \sum_{n;q} \langle \boldsymbol{\sigma}_n^{(q)} \rangle$$

$$\langle \boldsymbol{\sigma}_0^{(q)} \rangle = \left[\kappa_f \left\langle p_q p_0 \right\rangle - \rho_f \left\langle \mathbf{v}_q \cdot \mathbf{v}_0 \right\rangle \right] \mathbf{I} + \rho_f \left\langle \mathbf{v}_q \mathbf{v}_0 + \mathbf{v}_0 \mathbf{v}_q \right\rangle, \quad (19)$$

$$\langle \boldsymbol{\sigma}_n^{(q)} \rangle = \left[\kappa_f \left\langle p_q p_n \right\rangle - \rho_f \left\langle \mathbf{v}_q \cdot \mathbf{v}_n \right\rangle \right] \mathbf{I} + \rho_f \left\langle \mathbf{v}_q \mathbf{v}_n + \mathbf{v}_n \mathbf{v}_q \right\rangle,$$

where $\boldsymbol{\sigma}_n^{(q)}$ denotes the radiation stresses associated with the acoustic interaction, due to the product terms between the scattered pressure and velocity fields from the target object q and

those of object n. From Eq. (19), we can infer that the radiation force and torque depend on any factor that affects the scattering response of the objects. The factors that affect both the primary and interaction forces include the objects' size relative to the wavelength of the external wave, their geometry and dimensions, material properties relative to those of the surrounding fluid, internal structure of the objects, their capacity to absorb acoustic energy through internal dissipation or refraction, position and orientation in the external pressure field, and the wavefront of the external pressure wave. The factors that affect the interaction force are the relative distance between objects, their relative size difference, and the relative difference between the material properties of the objects. Here, we present two analytical formulations of the acoustic interaction force, the force potential[6,15] and Partial-Wave[5,7,8] models, with the goal of showing the con-

tribution of these physical factors, followed by the description of a numerical model based on Finite Element method (available in the Supplementary Materials).

2.3 Force potential formulation

The far-field approach, which leads to the Gor´kov force potential for the primary radiation force[2], is applicable to the acoustic interaction force by considering the incident field of an object being the sum of external and scattered fields of other objects[6,15], as shown in Eq. (17). By using the divergence theorem and conservation of momentum in the absence of any other external forces, the total radiation force integral can be simplified to

$$\mathbf{F}^{(q)} = -\int_{\Gamma_\infty} \langle \boldsymbol{\sigma}_q \rangle \cdot \mathbf{n}\mathrm{d}\Gamma = -\int_\Omega \boldsymbol{\nabla} \cdot \langle \boldsymbol{\sigma}_q \rangle \mathrm{d}\Omega$$

$$= -\int_\Omega \nabla \langle \kappa_f p_q \hat{p}_q - \rho_f \mathbf{v}_q \cdot \hat{\mathbf{v}}_q \rangle \mathrm{d}\Omega \qquad (20)$$

$$- \int_\Omega \rho_f \nabla \cdot \langle \hat{\mathbf{v}}_q \mathbf{v}_q + \mathbf{v}_q \hat{\mathbf{v}}_q \rangle \mathrm{d}\Omega.$$

Using $\nabla p = -\rho_f \partial_t \mathbf{v}$, $\langle p \partial_t \mathbf{v} \rangle = -\langle \mathbf{v} \partial_t p \rangle$, and $\mathbf{v} = \nabla \phi$, Eq. (20) becomes

$$\mathbf{F}^{(q)} = -\rho_f \int_\Omega \left\langle \hat{\mathbf{v}}_q \left(\nabla^2 \phi_q - \frac{1}{c^2} \partial_{tt} \phi_q \right) \right\rangle \mathrm{d}\Omega. \qquad (21)$$

Assuming the target object q is spherical in shape, the scattered velocity potential ϕ_q is expressed up to the dipole term as

$$\phi_q = -\alpha_q \frac{a_q^3}{3\rho_f} \partial_t \hat{p}_q \frac{e^{i(kr_q - \omega t)}}{r_q} - \frac{\beta_q}{2} a_q^3 \boldsymbol{\nabla} \cdot \left(\hat{\mathbf{v}}_q \frac{e^{i(kr_q - \omega t)}}{r_q} \right), \qquad (22)$$

where ω is the circular frequency of the wave, $k = \omega/c_f$ denotes the wavenumber, a_q is the radius of the object q, $\alpha_q = 1 - \kappa_q/\kappa_f$ and $\beta_q = (2\rho_q - 2\rho_f)/(2\rho_q + \rho_f)$ are the monopole and dipole coefficients[2,6,15], respectively, and r_q is the radial distance from the centre of sphere q. The incident acoustic density and velocity are $\hat{\rho}_q = \rho_0 + \sum_{n;q} \rho_n$ and $\hat{\mathbf{v}}_q = \mathbf{v}_0 + \sum_{n;q} \mathbf{v}_n$. Using the property of Green's functions for the wave equation $(\nabla^2 + k^2)(e^{ikr_q}/r_q) = -4\pi\delta(r; r_q)$ and integrating by parts, Eq. (21) can be solved analytically, and the total radiation force acting on object q becomes

$$\mathbf{F}^{(q)} = 2\pi a_q^3 \rho_f \left\langle \beta_q \hat{\mathbf{v}}_q \cdot \boldsymbol{\nabla} \hat{\mathbf{v}}_q \right\rangle_{\mathbf{x}=\mathbf{x}_q} - \frac{4\pi a_q^3}{3} \left\langle \alpha_q \hat{\mathbf{v}}_q \partial_t \hat{\rho}_q \right\rangle_{\mathbf{x}=\mathbf{x}_q}. \qquad (23)$$

where $\mathbf{x}_q$ denote the position vector of the centroid of object q. Further, using $\langle \mathcal{F} \partial_t \mathcal{G} \rangle = -\langle \mathcal{G} \partial_t \mathcal{F} \rangle$ and $\nabla \hat{p}_n = -\rho_f \partial_t \hat{\mathbf{v}}_n$, the above expression can be rewritten in terms of the incident pressure and velocity,

$$\mathbf{F}^{(q)} = 2\pi a_q^3 \rho_f \left\langle \beta_q \hat{\mathbf{v}}_q \cdot \boldsymbol{\nabla} \hat{\mathbf{v}}_q \right\rangle_{\mathbf{x}=\mathbf{x}_q} - \frac{4\pi a_q^3}{3} \kappa_f \left\langle \alpha_q \hat{p}_q \boldsymbol{\nabla} \hat{p}_q \right\rangle_{\mathbf{x}=\mathbf{x}_q}. \qquad (24)$$

This allows the total force potential G to be derived as

$$\mathbf{F}^{(q)} = -\boldsymbol{\nabla} G(\mathbf{x}_q),$$

$$G = \Omega_q \left[\frac{\kappa_f}{2} \left\langle \alpha_n \hat{p}_q \hat{p}_q \right\rangle - \frac{3\rho_f}{4} \left\langle \beta_n \hat{\mathbf{v}}_q \cdot \hat{\mathbf{v}}_q \right\rangle \right], \qquad (25)$$

where $\Omega_q = 4\pi a_q^3/3$. Substituting $\hat{p}_q = p_0 + \sum_{n;q} p_n$ and $\hat{\mathbf{v}}_q = \mathbf{v}_0 + \sum_{n;q} \mathbf{v}_n$ in Eq. (25) leads to

$$\mathbf{F}^{(q)} = \mathbf{F}_0^{(q)} + \sum_{n;q} \mathbf{F}_n^{(q)},$$

$$\mathbf{F}_0^{(q)} = \frac{3\Omega_q}{2} \rho_f \left\langle \beta_q \mathbf{v}_0 \cdot \boldsymbol{\nabla} \mathbf{v}_0 \right\rangle_{\mathbf{x}=\mathbf{x}_q} - \Omega_q \left\langle \alpha_q p_0 \boldsymbol{\nabla} p_0 \right\rangle_{\mathbf{x}=\mathbf{x}_q},$$

$$\mathbf{F}_n^{(q)} = \frac{3\Omega_q}{2} \rho_f \left\langle \beta_q \left[\boldsymbol{\nabla}(\mathbf{v}_n \cdot \mathbf{v}_0) + \mathbf{v}_n \cdot \boldsymbol{\nabla} \mathbf{v}_n + \frac{1}{2} \sum_{\substack{l=1 \\ l \neq n,q}}^N \boldsymbol{\nabla}(\mathbf{v}_n \cdot \mathbf{v}_l) \right] \right\rangle_{\mathbf{x}=\mathbf{x}_q}$$

$$- \Omega_q \left\langle \alpha_q \left[\boldsymbol{\nabla}(p_0 p_n) + p_n \boldsymbol{\nabla} p_n + \frac{1}{2} \sum_{\substack{l=1 \\ l \neq n,q}}^N \boldsymbol{\nabla}(p_n p_l) \right] \right\rangle_{\mathbf{x}=\mathbf{x}_q}, \qquad (27)$$

where $\mathbf{F}_0^{(q)}$ denotes the primary radiation force, and $\sum_{n;q} \mathbf{F}_n^{(q)}$ denotes the resultant interaction force acting on q. The pairwise interaction force $\mathbf{F}_n^{(q)}$ is derived as a partial component; however, the resultant force is important when a population of objects is studied. Both primary and interaction forces can be written in terms of force potential functions as

$$\mathbf{F}_0^{(q)} = -\boldsymbol{\nabla} G_0(\mathbf{x}_q), \qquad G_0 = \Omega_q \left\langle \frac{\kappa_f}{2} \alpha_q p_0^2 - \frac{3}{4} \rho_f \beta_q v_0^2 \right\rangle,$$

$$\mathbf{F}_n^{(q)} = -\boldsymbol{\nabla} G_n(\mathbf{x}_q),$$

$$G_n = \Omega_q \left\langle \kappa_f \alpha_q \left(p_n p_0 + \frac{1}{2} p_n^2 + \frac{1}{2} \sum_{\substack{l=1 \\ l \neq n,q}}^N p_n p_l \right) - \frac{3}{2} \rho_f \beta_q \left(\mathbf{v}_n \cdot \mathbf{v}_0 + \frac{1}{2} v_n^2 + \frac{1}{2} \sum_{\substack{l=1 \\ l \neq n,q}}^N \mathbf{v}_n \cdot \mathbf{v}_l \right) \right\rangle, \qquad (28)$$

where G_0 and G_n denote the force potential functions of the primary force and partial interaction force exerted by object n on the target q. The expressions for these scalar potentials indicate the dependence of acoustic interaction force on size, which appears as volume factor Ω, compressibility and density ratios, which determine explicitly α and β, and the external and scattered acoustic fields. The change of interaction force with respect to relative distance (d) between a source n and target q, as shown in Fig. 2(a), can be derived for the special case of a pair of identical particles along or normal to the propagation direction of a plane wave[6], corresponding to the direction of the pressure gradient, and has been shown[6,40] to be inversely proportional to $(kd)^4$. Furthermore, in this force potential formulation, the fully coupled scattering effects, up to the monopole-dipole approximation, are included in the calculation of the scattered fields of other objects, i.e., p_n and $\mathbf{v}_n$ in Eq. (28), while α_q and β_q only depend on the density and compressibility ratios[15]. At large interparticle distances, the effect of re-scattering is negligible[6,40] and the scattered fields from neighbouring object n can be calculated directly from α_n, β_n and the external fields p_0 and $\mathbf{v}_0$.

In Fig. 2, a collection of spherical bodies under an external

acoustic field is shown to cluster at various locations as a result of close-range interactions. Fig. 2(b) and (c) are the landscapes of interaction force potentials, obtained by moving the probe particle q around the fixed source particle n. The results are shown for a pair of spheres with the same size, cf. Fig. 2(b), and different sizes, cf. Fig. 2(c), to indicate the stronger interaction due to a volume increase of source sphere n.

To investigate the contribution of each of the terms in the interaction potential in Eq. (28), partial force potentials are shown in panels Fig. 2(d)-(i), for two source particles n_1 and n_2 and probe particle q. Comparing their range of variations in the close-range area, it can be seen that the interaction potential is dominated by $\langle p_n p_0 \rangle$ and $\langle \mathbf{v}_n \mathbf{v}_0 \rangle$ terms in Eq. (28), and denoted by the pair of indices $[0, n_1]$ and $[0, n_2]$ in Fig. 2.

2.4 Partial-Wave expansion formulation

A partial-Wave expansion or multipole series expansion is the method of describing a wave field by using the eigensolutions of the wave equation[5,7,8]. In this section, it is employed to present a series-based formulation for acoustic interaction force acting on spherical objects. This method is applicable to any size range, including comparable to or larger than the wavelength, since the force includes terms higher order terms such as quadrupole, octupole etc. The external velocity potential field at frequency ω, being well-defined at any point in a fluid domain, is written as

$$\phi_0 = e^{-i\omega t} \sum_{n,m} A_{lm} j_n(kr) Y_{lm}(\theta, \varphi), \qquad (29)$$

where j_n and Y_{lm} denote the spherical Bessel and spherical harmonics functions, respectively, (r, θ, φ) are the spherical coordinates with respect to the centre of expansion, A_{lm} denote the series coefficients, and $\sum_{n,m} = \sum_{l=0}^{\infty} \sum_{m=-n}^{n}$. The series expansions of the scattered and refracted potentials of object q are

$$\phi_q = e^{-i\omega t} \sum_{n,m} B_{lm}^{(q)} h_n(kr_q) Y_{lm}(\theta_q, \varphi_q),$$

$$\overline{\phi}_q = e^{-i\omega t} \sum_{n,m} C_{lm}^{(q)} j_n(kr_q) Y_{lm}(\theta_q, \varphi_q), \qquad (30)$$

where $(r_q, \theta_q, \varphi_q)$ are the spherical coordinates measured from the centre of object q, and h_n denotes the spherical Hankel function of the first kind that automatically satisfies the outgoing wave condition, which means scattered waves propagate away from the object. The coefficients $B_{lm}^{(q)}$ and $C_{lm}^{(q)}$ denote the scattering and refraction coefficients of object q, which are determined from the boundary conditions at the surface of the target object. The refraction potential $\overline{\phi}_q$ corresponds to the transmitted acoustic energy inside the particle. The boundary conditions on the at-rest surface of a compressible object q are[2,5,21,56]

$$\hat{\mathbf{v}}_q \cdot \mathbf{n}_q + \mathbf{v}_q \cdot \mathbf{n}_q = \overline{\mathbf{v}}_q \cdot \mathbf{n}_q + \mathbf{u}_q \cdot \mathbf{n}_q,$$

$$\hat{p}_q + p_q = \overline{p}_q, \qquad (31)$$

$$\mathbf{u}_q = \frac{i}{\rho_q \Omega_q \omega} \int_{\Gamma_q} (\hat{p}_q + p_q) \mathbf{n}_q d\Gamma,$$

where $\hat{p}_q$ and $\hat{\mathbf{v}}_q$ denote the incident pressure and velocity upon target object q, $\overline{p}_q$ and $\overline{\mathbf{v}}_q$ are the pressure and velocity of the refracted field inside object q, $\mathbf{n}_q$ denotes the unit vector normal to the surface of the object and pointing outwards, and $\mathbf{u}_q$ is the velocity of the rigid-body oscillation of the object under the action of the total acoustic pressure. The use of the Partial-Wave expansion and the orthogonality of the spherical harmonics were outlined in references[5,7,8,15,20,21], which provide a semi-analytical approach to solve the multi-scattering problem. This is useful in finding the scattering coefficients B_{lm} and C_{lm} of the series expansions for all objects at once, up to a given cut-off order L. By using the field relations in Eq. (3), and substituting Eq. (29) and (30) into Eq. (19), the stresses acting on object q are obtained. Then substituting the stresses into Eq. (15), the total acoustic radiation force and torque can be found. The integrations in Eq. (15) can be solved by applying the orthogonality properties of the spherical harmonics. These expressions are given for the Cartesian components of the total radiation force and torque as[5,8]

$$F_x^{(q)} + i F_y^{(q)} = \frac{iE_0}{2k^2} \sum_{l,m} \gamma_{xy} \left[S_l^{(q)} b_{l,m}^{(q)} b_{l+1,m+1}^{*(q)} + S_l^{*(q)} b_{l,-m}^{*(q)} b_{l+1,-m-1}^{(q)} \right],$$

$$F_z^{(q)} = \frac{E_0}{k^2} \Im \left[\sum_{l,m} \gamma_z S_l^{(q)} b_{l,m}^{(q)} b_{l+1,m}^{*(q)} \right],$$

$$T_x^{(q)} + i T_y^{(q)} = -\frac{E_0}{2k^3} \sum_{l,m} \zeta_{xy} \left[\hat{S}_l^{(q)} b_{l,m}^{(q)} b_{l,m+1}^{*(q)} + \hat{S}_l^{*(q)} b_{l,-m}^{*(q)} b_{l,-m-1}^{(q)} \right],$$

$$T_z^{(q)} = -\frac{E_0}{k^3} \Re \left[\sum_{l,m} \zeta_z \hat{S}_l^{(q)} b_{l,m}^{(q)} b_{l,m}^{*(q)} \right],$$

$$S_l^{(q)} = s_l^{(q)} + s_{l+1}^{*(q)} + 2 s_l^{(q)} s_{l+1}^{*(q)}, \quad \hat{S}_l^{(q)} = \left(1 + s_l^{(q)} \right) s_l^{*(q)},$$

$$\gamma_{xy} = \sqrt{\frac{(l+m+1)(l+m+2)}{(2l+1)(2l+3)}}, \quad \zeta_{xy} = \sqrt{(l-m)(l+m+1)},$$

$$\gamma_z = \sqrt{\frac{(l-m+1)(l+m+2)}{(2l+1)(2l+3)}}, \quad \zeta_z = m,$$

$$(32)$$

where $B_{lm}^{(q)} = s_l^{(q)} b_{lm}^{(q)}$. The scaling factors $s_l^{(q)}$ are independent of order m for the case of spherical particles, and these are obtained from the boundary conditions for compressible spheres. The terms $b_{lm}^{(q)}$ are the series coefficients of the incident velocity potential on sphere q,

$$\hat{\phi}_q = e^{-i\omega t} \sum_{n,m} b_{lm}^{(q)} j_n(kr_q) Y_{lm}(\theta_q, \varphi_q). \qquad (33)$$

The resultant interaction force and torque are obtained by subtracting the primary ones from the total force and torque from Eq. (32),

$$\sum_{n;q} \mathbf{F}_n^{(q)} = \mathbf{F}^{(q)} - \mathbf{F}_0^{(q)},$$

$$\sum_{n;q} \mathbf{T}_n^{(q)} = \mathbf{T}^{(q)} - \mathbf{T}_0^{(q)}, \qquad (34)$$

where $\mathbf{F}_0^{(q)}$ and $\mathbf{T}_0^{(q)}$ are the primary radiation force and radiation torque and obtained by substituting $s_l^{(q)} = A_{lm}^{(q)}/B_{lm}^{(q)}$ into Eq. (32).

The force and torque expressions in Eq. (32) are valid for spherical objects of arbitrary size. For numerical calculations using this method, the Partial-wave series, Eqs. (29)-(30) needs to be truncated to an order that is determined by the same factors that affects the scattering response of an object, including its relative distance to others in the fluid[5–8,20]. These truncated series with N terms imply that the multiple scattering solution for a population of objects is accurate up to the Nth re-scattering order[7]. For sub-wavelength objects within the Rayleigh limit $ka \ll 1$, the force and torque series can be truncated at $l = 2$, which implies the dominant contributions from monopole and dipole scattering modes of the target objects. For larger objects, accurate estimates of the force and torque are obtained by including higher order scattering coefficients $l = 3, 4, \cdots, L$. However, they provide no explicit relation between the physical factors and the acoustic interaction force. The dependence on the relative distance between the objects is implicitly included in the coefficients of multipole translation and rotation[5,7,8]. Several attempts were made to derive explicit equations from the force expressions for a simple configuration of a pair of spherical objects along and normal to the direction of a plane wave[5,7]. Nonetheless, these expressions give the radiation force and torque directly from the scattering coefficients, which are obtained by solving the multiple scattering problem.

2.5   Numerical modelling

The acoustic interaction force acting on spherical objects in a standing wave was widely investigated based on the aforementioned theoretical approaches. However, numerical modelling offers a more generic approach for studying the effects of geometry, material properties and thermo-viscous losses beyond the applicability limit of analytical models. Finite Element models, which account for coupled scattering from a number of objects by solving the acoustic wave equation Eq. (4) and imposing outgoing conditions on the scattered waves, were proposed to examine numerically the acoustic interaction force[40,57]. The simulation provides a direct solution of the total acoustic pressure and velocity fields, from the superposition of the external and scattered components. The total acoustic radiation force can be obtained using the surface integral over a fictitious surface enclosing the target object, given by Eq. (15). The acoustic interaction force is then calculated by subtracting the primary force from this total radiation force.

A Finite Element model enables estimation of the acoustic interaction force from the scattered pressure field at the post-processing level, provided that viscosity-induced acoustic streaming effects are negligible. The compressibility of the objects and the acoustic refraction can be coupled with an exterior acoustic scattering model[38,58], to incorporate the effects of the object's material properties. In a Finite Element model, the coupled scattering and deformation of an object in the acoustic field are accounted for automatically for all orders of scattering that can be captured by a certain mesh size, as compared to the force

potential model in Sec. 2.3 and the Partial-Wave expansion solution in Sec. 2.4, which only include several orders of scattering modes for numerical evaluation. The Finite Element model also provides a robust approach to investigate the effects of external acoustic fields with arbitrary wavefront on the interaction between objects of different shapes. Thermo-viscous effect can be incorporated in the numerical model to simulate the change in scattering and viscous dissipation. However, this numerical approach is not valid for objects in contact with each other, which can be solved by using other methods such as those based on Partial-Wave expansions, as outlined in Sec. 2.4. Another drawback of the Finite Element model is the computational cost of a three-dimensional full-wave simulation that increases significantly as more objects are considered in the acoustic field, particularly when their surface-to-surface distance is much smaller than their dimensions. A COMSOL implementation of this Finite Element model of acoustic interaction force for sound-hard spheres in an ideal fluid, provided as Supplementary Material, has been used to validate the results of the analytical solution in Sec. 2.4.

2.6   Modelling results

Fig. 3(a) shows the numerical results of acoustic interaction force for two spheres located symmetrically with respect to a pressure node at $z/a_s = 0$ in a plane standing wave, using a 3D acoustic scattering simulation conducted with COMSOL Multiphysics. The results are in a good agreement with those shown in Fig. 3(b) of reference[7], obtained from the Partial-Wave expansion method, except for the case of spheres in contact, which are marked by red crosses in Fig. 3(a). These forces can be decomposed into components along and normal to the centre-to-centre line, as shown in Fig. 3(b), to demonstrate the coupled rotational motion due to the tangential components, in addition to the radial repulsion-attraction between the spheres. This is one distinguishing factor of acoustic interaction forces, compared to other forms of interaction e.g., those generated by an electric field. This pattern of interaction in terms of direction of forces for a pair of identical spheres is independent of their locations in a plane standing wave, and only the magnitude of the interaction forces varies with their location relative to the pressure node.

Acoustic interaction forces are usually equal and opposite for identical objects, i.e., with same modes of scattering, as shown in Fig. 4(a) and (b) for two similar polystyrene beads in water. In this case, the scattering is dipole-dominant. For the case of non-identical spheres, with material properties as shown in Fig. 4(c) and (d), the interaction forces applied to each of the objects are different both in terms of direction and magnitude. This non-reciprocity is another distinguishing feature of acoustic interaction, which originates from the nonlinear second-order acoustic effects. Considering these two features, rotational coupling and non-reciprocity, close-range agglomeration of objects in an acoustic field can be described through a pair-wise tracking of interactions for population of objects with size, shape or material heterogeneity[10,21,59–62].
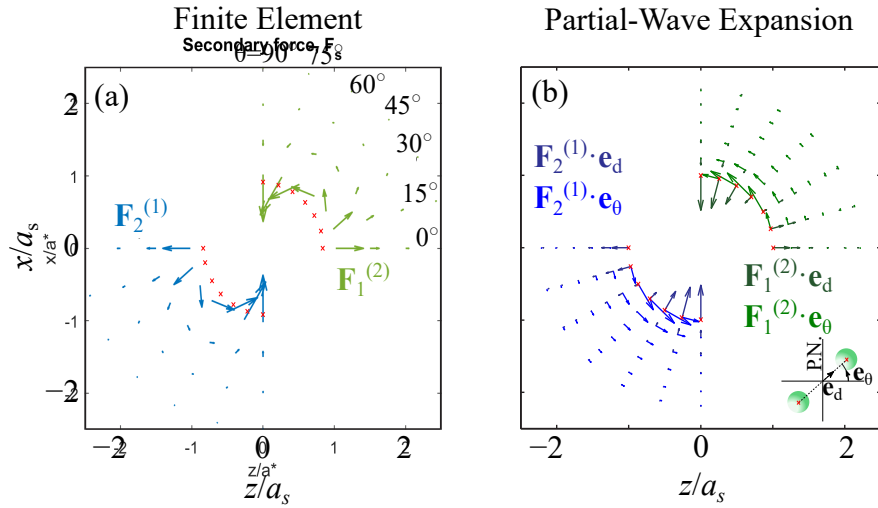
Fig. 3 Acoustic interaction forces acting on a pair of spherical objects at symmetric locations at the sides of a pressure node of a plane standing wave, obtained using (a) a Finite Element model and (b) a semi-analytical Partial-Wave expansion [7] (Reprinted with permission from Shahrokh Sepehrirahnama S., Lim K.-M., Chau F.S. Numerical study of interaction force acting on rigid spheres in a standing wave, The Journal of the Acoustical Society of America 137, 2614. Copyright 2015, Acoustic Society of America, https://doi.org/10.1121/1.4916968). The decomposition of the interaction force into radial and tangential components, denoted $\mathbf{F} \cdot \mathbf{e}_d$ and $\mathbf{F} \cdot \mathbf{e}_\theta$, respectively, with $\mathbf{e}_d$ and $\mathbf{e}_\theta$ being the radial and tangential basis vectors, respectively, is shown in panel (b). These theoretical results are obtained for the limit of sound-hard and immovable spheres with $ka \approx 0.03$ for an ideal fluid, for which viscosity effects on scattering and streaming are neglected. In practical applications, the size index of $ka \approx 0.03$ relates to manipulation of 5 μm particles using 1.5 MHz ultrasonic wave. The case of touching spheres, shown by the cross markers, can be only solved using the semi-analytical approach; since the volume of elements in the Finite Element model should be non-zero to avoid modelling-related singularities.
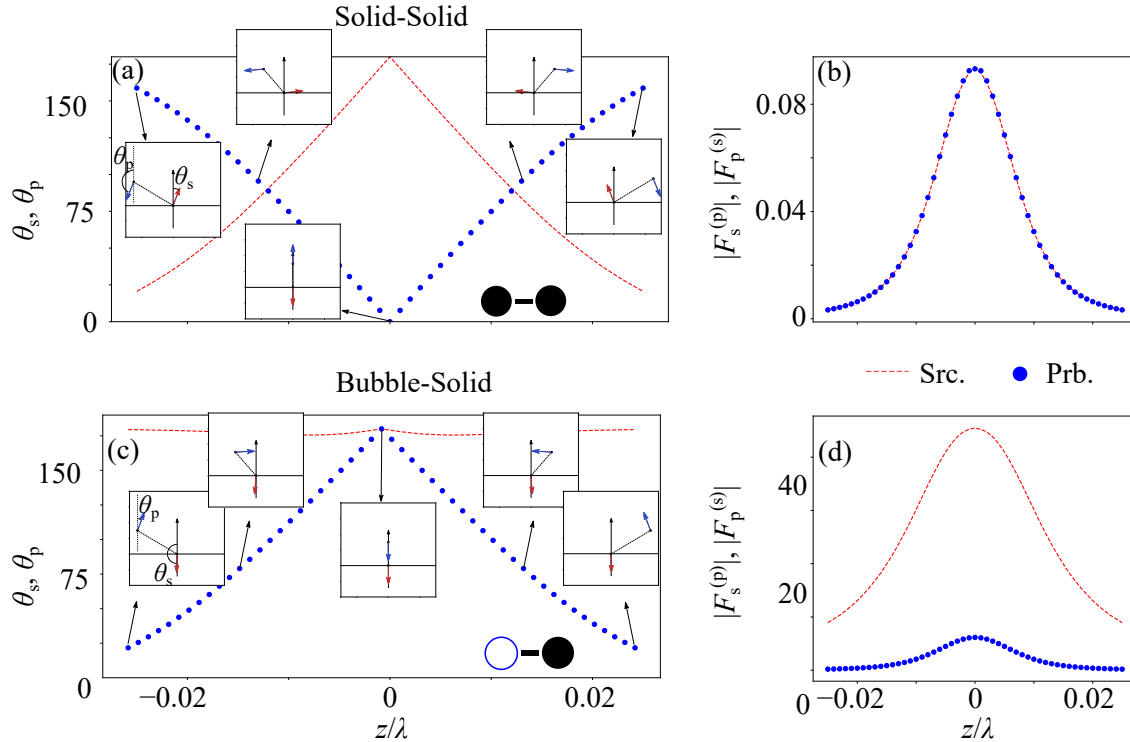

Fig. 4 Reciprocity analysis of interaction forces acting on each object due to the presence of the other for (a)-(b) two identical solid spheres with (dipole-dominant scattering responses) and (c)-(d) non-identical ones, which are a gas bubble (monopole-dominant scattering responses) and a solid sphere (dipole-dominant scattering response). The size index of the spheres is $ka \approx 0.03$, similar to those in Figs. 2 and 3, and the results are obtained at the limit of ideal fluid, governed by Eqs. (7), (13), and (15). Panels (a) and (c) show the change in the force angle when the source is fixed and the probe is shifted horizontally with an offset distance. In the case of the non-identical pair, the source is the gas bubble. Unlike electrical forces, acoustic interaction forces satisfy the Newton's third law only for identical objects. The results are shown for plane standing waves and the probe is placed at the pressure node. Reprinted figure with permission from Sepehrirahnama S., Lim K.-M., Physical Review E, 102, 043307, 2020. Copyright (2020) by the American Physical Society, https://doi.org/10.1103/PhysRevE.102.043307.

2.7 Limitations of the ideal-fluid assumption

The theoretical models presented in subsections 2.2-2.6 are obtained for an ideal fluid, i.e., neglecting thermo-viscous dissipation and its contribution to acoustic streaming. Only the radiation-related stresses are used to determine the acoustic forces, i.e., the primary forces and the interaction forces. Within this limit, the Partial-Wave expansion model, Eqs. (32)-(34), applies to any particle size and frequency, as long as sufficient terms are used in the estimate of the multipole series and as long as the wave propagation is governed by Eq. (4). The force potential model of acoustic forces, Eqs.(28), only applies to particles in the Rayleigh scattering limit of $ka \ll 1$, an assumption valid for $ka < 0.3$ in numerical calculations [7,63], based on the comparison of primary force between these models [7,13,27]. Nevertheless, the size considerations in the two models for an ideal fluid can provide an estimate of interaction force direction and magnitude, based on which the theoretical results and experimental measurements can be compared.

These models can also be used for calculation of the primary force in a viscous fluid [19,27], due to the viscous losses becoming negligible at distances of several wavelengths away from an object and its thermal and viscous boundary layers. At such distances the fluid is well approximated by a lossless medium [19,64]. This implies that objects can be modelled by their equivalent counterparts, by adding the viscous layer thickness to their size, and giving them equivalent material properties such that their scattering response is the same as the original object in a viscous fluid. This modelling approach provides a corrected estimate of the acoustic radiation force and streaming effects by accounting for thermo-viscous dissipation in the vicinity of the objects' surface [19,64]; however, it is not applicable to cases with strong viscous-induced flow. [28]. Finally, these analytical models provide an estimate of the acoustic radiation forces, neglecting the hydrodynamic effects of acoustic streaming, as a reference and to demonstrate the relative behaviour of particles using acoustic interaction force. If viscosity effects are included, the dynamics of the particles can be modelled more accurately. We will review the influence of viscous dissipation in Sec. 5 from the viewpoint of the acoustic interaction force.

The acoustic radiation force results from radiation stress, cf. Eq. (15) as a coupled fluid-structure effect, acting on the exterior surface [13,15]; hence, it scales with the square of the nominal size of an object [2,13]. For objects much smaller than the wavelength, exhibiting Rayleigh scattering [2], the magnitude of the acoustic force can become comparable to the weight and buoyancy forces. Such small objects are commonly referred to as particles, implying that they behave dynamically like point masses. However, recent studies showed that the classical particle view is insufficient to describe the dynamics of certain objects, due to the relation between the geometry and the acoustic radiation torque [65–67] and limitations of force models based on symmetric shapes such as spheres, spheroids, disks and cylinders [18]. Shape effects can be incorporated into the models presented in Sec. 2.3, using acoustic polarizability and Willis coupling, or by solving for multipole coefficients numerically, as presented in Sec. 2.4. Similar to the interaction forces, there are interaction torques between particles with asymmetries [11], which have yet to be studied in detail. For non-spherical particles there exists a preferred orientation due to the action of radiation torque. To further extend the presented models, it is necessary to include the effects of the interaction torque for a population of non-spherical particles, which would also represent a more realistic model of biological cells.

3 Experimental measurements

Experimental measurement of radiation force in acoustophoresis is performed indirectly, typically the force is extracted from the observed trajectories of the particles. This relies on a descriptive model to analyse the particle motion. The equations of motion indicating this dynamic model are solved for the radiation force, as one of the forces acting on the particles. Direct measurement of acoustic radiation force is also possible in a hybrid opto-acoustic setup, where the stiffness of the optical trap is used to calculate the acoustic radiation force from the small displacement of a particle [68–71]. The small wavelength of the optical source results in finer spatial resolution of the radiation forces. However, it requires more instrumentation, a laser source, and precise calibration. More importantly, the measurement of acoustic interaction by hybrid opto-acoustical methods is yet to be explored.

In this section, the requirements for obtaining of acoustic interaction force from the trajectories of particles are outlined. As the particles are small and their intertia is negligible compared to the external force and the fluid drag, the equations of motion can be obtained with the quasi-static assumption [12]. A two sphere-model will be used to describe the equations of motion in the quasi-static regime, including acoustic and hydrodynamic forces. The acoustic interaction forces from the experimental measurements will be presented and compared with the theoretical predictions. The quasi-static motion can be used to describe the dynamics of particles that have negligible inertia. This is a phenomenological model describing the slow changes of the scatterers' positions under an acoustic streaming field, compared to the time period of the external acoustic wave, and is valid for ultrasound frequencies in practical applications [3,13,24,25,54]. Such quasi-static motion requires a balance between acoustic radiation forces and the hydrodynamic resistance (drag), which can be due to a background mean flow, i.e., relative motion of the fluid to moving objects from before the acoustic excitation, and acoustic streaming [72,73]. In addition, the motion of a particle in a fluid generates a flow field around neighbouring objects which causes them to hydrodynamically interact [74]. In the presence of other force fields such as electrostatic or the pressure gradient of a background mean flow, the contribution from the hydrodynamic forces will change according to the resultant effects of acoustic and other external forces.

3.1 Experimental setup and procedure

Particle tracking has been a major technique in acoustophoretic experiments to characterise acoustofluidic devices and to conduct measurements [72,73]. It can be used to measure and quantify acoustic radiation forces acting on particles subject to an ultrasound field. Fig. 5(a) presents a schematic of a setup used

in acoustophoretic experiments[12], which we describe in detail here. The corresponding photography is presented in Fig. 5(b), where the microfluidic channel is a glass capillary viewed from the top via microscope[12], which tracks the motion of beads under acoustic radiation forces. Similar microfluidic channels can be manufactured from a silicon wafer[40,72,73], a steel plate[9], or PDMS enclosed in an Aluminium housing (hybrid metal-polymer design)[75]. The advantage of the glass capillary is the smoother surfaces compared to channels that are etched or cut from silicon and metal. Glass capillaries have also been used in measurements of membrane stiffness of biological cells[38,58]. Although it has been shown that micron-sized irregularities on the channel wall may result in a slightly weaker acoustic pressure field, the effect was found to be negligible[76]. Also, these manufacturing-related issues of surface roughness can be resolved by using hybrid metallic-polymer microfluidic fabrication, which is also a cost-effective manufacturing approach that leads to much smoother channel walls[75].

The basic experimental set-up consists of an optical microscope (Leica DMLM), charge-coupled device (CCD) camera, computer, external light source (Leica CLS 150X), signal generator (Agilent 33120A) and syringe pump[12]. To monitor the signal, temperature and other experimental conditions, an oscilloscope (Hewlett-Packard 54600A), high frequency multimeter (Agilent 3458A) and thermistor (MP-2444, TE Technology) are used[12]. A power amplifier (e.g., NF HSA 4101) is used to amplify the output of the signal generator to drive the piezo transducer. At high power levels, the piezo transducer generates excessive heat due to hysteresis and the temperature of the device may get too high for the experiment. Therefore, the device includes a cooling system consisting of a heat sink, Peltier module (from TE Technology) and temperature control unit (TC-48-20, TE Technology) as shown in Fig. 5(b)[38]. Electrical connections are shown as black dashed lines, and the fluid network is shown as blue solid lines in Fig. 5(a).

The experiment for acoustic interaction forces requires tracking of particles in a fluid. Particle motion is recorded with a CCD camera connected to the microscope and image processing software (e.g., Nikon NIS Elements BR scientific image processing software)[38]. The digital media files are stored in a computer and post processed using image processing software, e.g., Tracker[77], to extract the trajectories of the particles from the media files[12,73].

Experimental measurements for the interaction force have been conducted with the specimen solution of polystyrene spheres in water[9,12,40]. Additionally, fluorescent particles can be used as they are better for the tracking[12]. It has been shown that precisely two spheres can be trapped in the field of observation by using a low concentration of polystyrene sphere suspensions[12]. This low concentration suspension was prepared by diluting the suspension mix, which resulted in about 10 to 100 particles per microlitre of the specimen solution for $7.81 - 12.32$ μm diameter particles. The specimen solution was monodisperse, i.e., only one size of the particle (7.81 μm, 9.9 μm or 12.32 μm) was present for any observation in the experiment. The size of the particles was selected based on the cross section of the channel, which is 40 μm $\times$ 400 μm and the strength of the input signal. Select-

ing a larger diameter of the particle may lead to difficulty in injecting the particles into the shallow channel and will also result in extra drag from the top and bottom surfaces of the channel. However, smaller particles require a high power input signal for sufficient signal to noise ratio, which results in more heat dissipation from the PZT transducer and the temperature increasing rapidly in the channel. The setup was designed to include a single pressure node in the 400 μm width, at the 1.875 MHz excitation frequency. The input signal to the PZT transducer was set to 60 V peak-peak. The selection of particle sizes (7.81, 9.9 and 12.32 μm) is a compromise between these considerations. During the specimen solution preparation, a small amount (about $0.2 - 0.3\%$ of the total volume) of Tween 20, a non-ionic aqueous solution, was added.[12]. Tween 20 is a surfactant which is used to reduce the surface tension of the buffer fluid[78]. A glass surface becomes hydrophilic when treated with Tween 20 surfactant[79], which prevents the beads from sticking to the glass surface of the fluid chamber. Furthermore, the concentration of Tween 20 is very low in the specimen solution, and it barely alters the mechanical properties, such as dynamic viscosity of the water medium[80]. As the measurements of the interaction force were conducted for non-touching particles, the influence of this additive is negligible in interaction force measurements.

3.2 Energy density measurement

The energy density E_{ac} of the incident acoustic standing wave in the resonating chamber is the key quantity to obtain. The amplitude of the acoustic pressure is directly proportional to the square root of the acoustic energy density, which is used as the input in the numerical simulations and theoretical calculations. Therefore, it is important to measure the acoustic energy density E_{ac} accurately to reduce discrepancies between the theoretical calculations and experimental results. Generally, the estimation of E_{ac} involves tracking of spherical particles or beads under the influence of the primary radiation force. By the quasi-static approximation, the primary radiation force ($\overline{F}_0$) is balanced by the Stokes drag[72,73],

$$\overline{F}_0 = 6\pi\mu au, \quad (35a)$$

$$4\pi a^3 k\, E_{ac}\, \Phi\, \sin(2kh) = 6\pi\mu au. \quad (35b)$$

where $\Phi = \frac{\alpha}{3} + \frac{\beta}{2}$, a, k, u, h and μ are the acoustic contrast factor, radius of the spherical particle, wavenumber, speed of the particle, distance from the pressure node and dynamic viscosity of the host fluid, respectively[56]. In the above expression, the primary radiation force is always acting towards the pressure node; hence, h is the distance from the pressure node to the particle centre and is always positive. The closed form of primary radiation force $\overline{F}_0$ in Eq. 35b is valid up to the dipole approximation of the scattered pressure fields. Also, this expression is valid under the assumptions that the sphere is much smaller than the wavelength under investigation, and considering a perfectly planar standing wave within an unbounded fluid domain.

The experimentally observed trajectory in the direction of the field is fitted with a theoretical trajectory using a least-squares
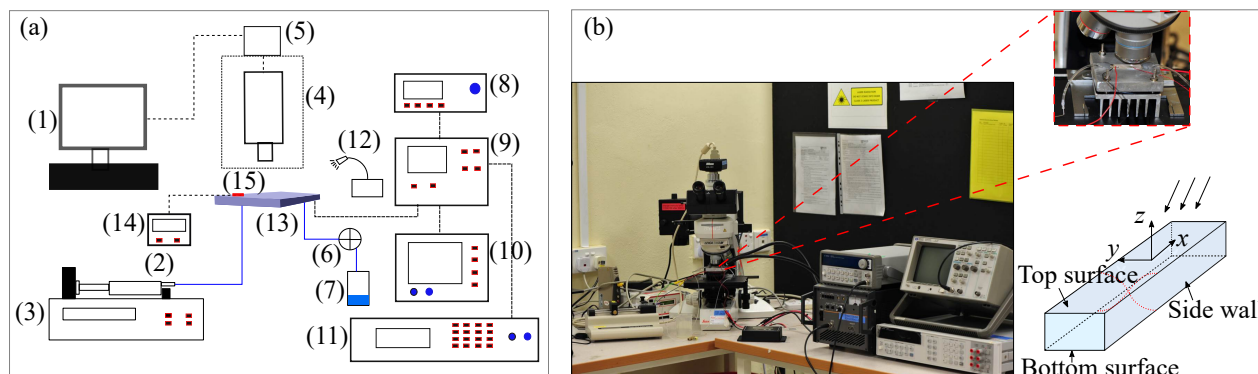
Fig. 5 (a) Schematic of an acoustophoretic experimental set-up: (1) computer, (2) syringe, (3) syringe pump, (4) microscope, (5) CCD, (6) valve, (7) waste flask, (8) signal generator, (9) amplifier, (10) oscilloscope, (11) multimeter, (12) light source, (13) microfluidic device, (14) temperature control unit, and (15) thermistor. (b) Laboratory set-up for the acoustophoretic experiment. Reprinted figure with permission from Mohapatra A. R., Sepehrirahnama S., Lim K.-M., Physical Review E, 97, 053105, 2018. Copyright (2018) by the American Physical Society. http://dx.doi.org/10.1103/PhysRevE.97.053105.

method of Eq. (35b), where E_{ac} is the unknown parameter[72,73]. The estimation of E_{ac} from the least-squares method is accurate, when the particle is isolated, i.e., the hydrodynamic interaction and also the acoustic interaction force induced by other particles can be neglected due to their large separation. For multiple particles in proximity, the dynamics become complicated and the error in the above model, Eq. (35b) and least-squares method increases. For the above model in Eq. (35b), the estimation of E_{ac} is required to analyze all the particles simultaneously with hydrodynamic and radiation interaction forces. Hence, the measurement of acoustic energy density using the motion of probing particles should ideally be performed using a single isolated particle[2,9,12,72]. For particles much smaller than the cross-section of a fluidic channel, the Stokes drag equation is sufficient to include the hydrodynamic effects. However, this is only applicable when the particle is trapped in a location where the streaming-induced drag force from the fluid domain walls is negligible, e.g., when particles are trapped at the pressure node of a plane standing wave and far away from the walls. Otherwise, the contribution of the channel walls to the hydrodynamic effects becomes significant[12,81]. In a large population, isolating a single particle to estimate the energy density is challenging. This is yet to be fully explored, one possible approach is to use a coupled model of hydrodynamic interaction to obtain a more accurate estimation of the energy density.

In the acoustic interaction force experiment of Ref.[12], the measurements were performed for a pair of isolated particles. The motion of a particle is influenced by the presence of the other particle only. The effect of the acoustic interaction force on the estimation of E_{ac} can be neglected in this case, since the primary radiation force is much higher than the acoustic interaction force. Nonetheless, the hydrodynamic force should be included for the correct estimation of the drag and consequently of E_{ac}. The motion of a particle in the fluid induces a Stokes-type flow in addition to the background or streaming flows. For the two particles moving parallel to each other towards the pressure node, the total hydrodynamic interaction assists the motion of the particles, resulting in their dynamics being determined by the sum of

the primary radiation and the hydrodynamic interaction forces. Therefore, the inclusion of hydrodynamic interaction will result in a smaller E_{ac} estimation compared to the case without hydrodynamic interaction, e.g., using Stokes drag in case of a single particle[12].

3.3 Experimental observations
The direct evidence of the acoustic interaction force can be observed from the trajectories of the particles. The interaction force is stronger at short ranges. Therefore, to observe its effect, the particles should be in close vicinity. Fig. 6 presents the trajectories of a pair of 12.32 μm diameter polystyrene beads subject to an ultrasound standing wave[12]. The normalised centre-to-centre distance between the beads (r/a) decreases with time, as shown in Fig. 6(c), due to the attractive nature of the interaction force in this configuration[27]. The two beads finally meet at the pressure node plane, i.e., the middle of the channel, shown as dashed line in Fig. 6(a) and (b). To calculate the interaction force from experimental observations, the trajectories of the beads near the pressure node were chosen. Near the pressure node, the primary radiation force becomes negligible, and the overall dynamics of the beads depend primarily on the interaction force[12]. Fig. 6(d) and 6(e) present the trajectories in x and y from the experiment and the quadratic fit (solid line) to the experimental observations. The quadratic fit is useful to calculate the velocity of the beads by differentiation during the calculation of the interaction force. The least-squares method or curve fitting tool in MATLAB can be used for the quadratic fit of the experimental observations of the trajectory. This analysis was performed for particle pairs of equal size and for all three diameters (7.81, 9.9 and 12.32 μm). The measurement of the acoustic interaction force for all three sizes is presented in the following section.

3.4 Extraction of the interaction force
Next, a model is developed for the two-bead system to calculate the unknown interaction force from the trajectories of the beads. Fig. 7 presents a two sphere model for the calculation of
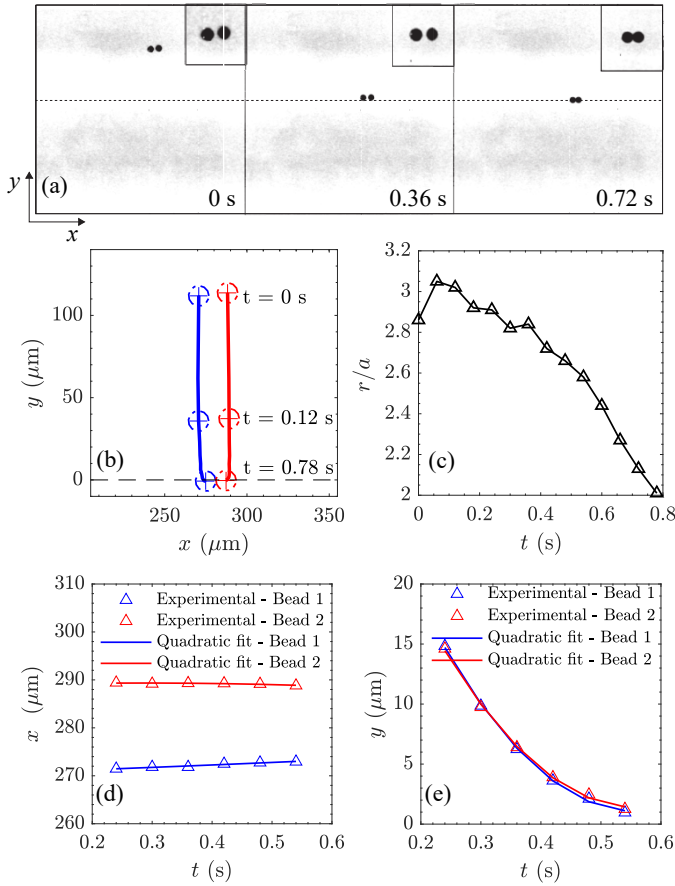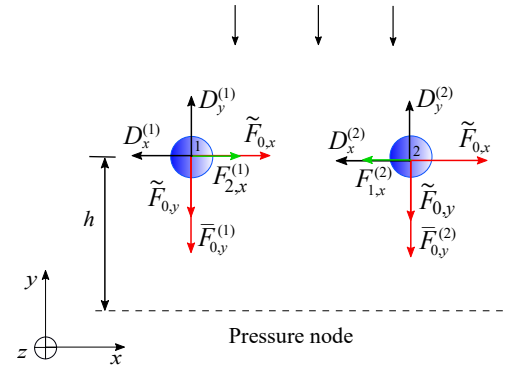
Fig. 7 Two sphere model for calculation of the acoustic interaction force[12]. Reprinted figure with permission from Mohapatra A. R., Sepehrirahnama S., Lim K.-M., Physical Review E, 97, 053105, 2018. Copyright (2018) by the American Physical Society. http://dx.doi.org/10.1103/PhysRevE.97.053105.

Fig. 6 Experimental observations of a pair of 12.32 μm polystyrene beads[12]. (a) Snapshots of the beads in ultrasound, (b) the trajectories during the expetiment, (c) normalised centre-to-centre distance (r/a). (d) and (e) Experimental and quadratic fit of the trajectories in x and y. Reprinted figure with permission from Mohapatra A. R., Sepehrirahnama S., Lim K.-M., Physical Review E, 97, 053105, 2018. Copyright (2018) by the American Physical Society. http://dx.doi.org/10.1103/PhysRevE.97.053105.

the interparticle radiation force, where the beads are approaching the pressure node[12]. The beads in the fluid medium experience acoustic radiation force induced by the ultrasound standing wave and the fluid drag. The acoustic radiation force is separated into the primary radiation force (F_0) and the acoustic interaction force ($F_2^{(1)}$ and $F_1^{(2)}$ for the interaction force acting on bead 1 due to bead 2 and on bead 2 due to bead 1, respectively). The primary radiation force can be further separated into nominal or mean primary radiation force ($\overline{F}_0$) and the perturbation of the primary radiation force ($\widetilde{F}_0$). For the case of a sphere of radius a at a distance h from the pressure node of the standing wave, the time-averaged magnitude of the radiation force[56], $\overline{F}_0$ is given by

$$\overline{F}_0 = 4\pi a^3 k\, E_{ac}\, \Phi\, \sin(2kh). \tag{36}$$

The perturbation part of the primary radiation force, $\widetilde{F}_0$ is due to the imperfections in the resonance cavity and the non-uniform energy transfer from the piezo transducer to the resonance cavity[12]. $\widetilde{F}_0$ is treated as an unknown in the model because of the difficulty to predict it. The total primary radiation force in the

model is

$$F_0 = \overline{F}_{0,y} + \widetilde{F}_{0,x} + \widetilde{F}_{0,y}, \tag{37}$$

where x and y in the subscript denote the components in the Cartesian coordinate. When the beads are close, the perturbation part of the primary radiation force, $\widetilde{F}_0$ is assumed to be the same for both beads[12].

The acoustic interaction force can be resolved into two components: radial and tangential. The tangential component is negligible when the centre-to-centre line of the beads is nearly perpendicular to the incident wave direction and the beads are close to the pressure nodal plane ($h < 30\mu m$)[12]. Therefore, the interaction forces are only in the radial direction (x-direction) in this model, and they are denoted as $F_{2,x}^{(1)}$ and $F_{1,x}^{(2)}$.

In the above quasi-static model, the inertia force is negligible and the external forces on the beads are balanced by the fluid drag. It is recommended to include hydrodynamic interaction in the model for the measurement of acoustic interaction force[12]. The translational velocities (U) of the two spheres in an infinite quiescent fluid domain are proportional to the total drag forces (D)[12] through

$$\begin{pmatrix} U_i^{(1)} \\ U_i^{(2)} \end{pmatrix} = \frac{1}{6\pi\mu a} \begin{bmatrix} \delta_{ij} & C_{ij} \\ C_{ij} & \delta_{ij} \end{bmatrix} \begin{pmatrix} D_j^{(1)} \\ D_j^{(2)} \end{pmatrix}, \tag{38}$$

where δ_{ij} is the Kronecker delta, and the superscript in parentheses indicates the sphere involved. The coefficient C_{ij} for two spheres separated by centre-to-centre distance r in the xy plane is

$$C_{ij} = \frac{3a}{4r^5} \begin{bmatrix} r^4 + \frac{r^2 a^2}{3} + (r^2 - a^2)\hat{x}^2 & (r^2 - a^2)\hat{x}\hat{y} \\ (r^2 - a^2)\hat{x}\hat{y} & r^4 + \frac{r^2 a^2}{3} + (r^2 - a^2)\hat{y}^2 \end{bmatrix}. \tag{39}$$

The indices i and j take on the corresponding direction x or y accordingly. This model can be extended to a population of N particles, accounting for collisions, to model the process of agglomeration[10,21].

From the free body diagram (Fig. 7), the equations of motion

of the two beads are obtained as

$$\widetilde{F}_{0,x} + F_{2,x}^{(1)} - D_x^{(1)} = 0 \tag{40a}$$

$$-\overline{F}_{0,y}^{(1)} - \widetilde{F}_{0,y} + D_y^{(1)} = 0 \tag{40b}$$

$$\widetilde{F}_x^P - F_{1,x}^{(2)} - D_x^{(2)} = 0 \tag{40c}$$

$$-\overline{F}_{0,y}^{(2)} - \widetilde{F}_{0,y} + D_y^{(2)} = 0 . \tag{40d}$$

As the two beads are identical to each other, $F_{2,x}^{(1)} = F_{1,x}^{(2)}$. From the above equations of motion, the interaction force between the two beads is given by $F_{2,x}^{(1)} = F_{1,x}^{(2)} = \frac{1}{2}(D_x^{(1)} - D_x^{(2)})$ [12].

Similar dynamic models have been reported in [9,40,82] for the calculation of interaction forces. The balance of forces between the acoustic radiation force and drag is common to all of these models. The small variations among the models are due to the different experimental conditions and procedures. Including the hydrodynamic interaction for the calculation of the total drag is important for the close-range estimation of the interaction force [12]. Also, the inclusion of buoyancy, and gravity are considered, when the direction of the standing wave and the motion of the particles in the experiment are aligned with them. For polystyrene beads, with slightly higher density than water, the effect of gravity can be ignored. Moreover, the motion of the beads is in the horizontal plane for the present model; hence, the forces in the vertical direction have been ignored.

The interaction force between two equal polystyrene beads has been measured and compared with the theoretical results in Fig. 8(a) [12]. The interaction force has been normalised to $F_{2,x}^{(1)}/(E_{ac}k^4a^6)$ to factor out the size effect of beads, which results in a slope of about four on a log-log scale. The value of E_{ac} in the normalisation is the average of the estimates from the individual bead trajectories in the pair. In Fig. 8, Theoretical-1 was generated from the analytical formula derived by Silva and Bruus (2014) [83] using up to dipole approximation and Theoretical-2 was obtained from the numerical simulation similar to Sepehrirahnama *et. al.* (2015) [27] with the Partial-Wave expansion up to fifth order. Both theoretical results were obtained by including the compressibility of the particles.

Fig. 8(b) presents the linear fit of the experimental data using MATLAB. These trends are in general agreement with the theoretical lines, which consider only the leading dipole terms in the interaction force [83]. The experimental values are larger than those given by theory, although the slopes of the experimental trend lines are close to those from theory. This could be due to the effects of viscosity and acoustic streaming at close-range, which result in higher interparticle radiation forces [20]. The different between theoretical and experimental results has a contribution from the wall effect in a shallow channel [12,74]. The calculation is based on the quasi-static equilibrium of the particles in an infinite fluid domain. However, in the experiment the acoustic chamber is a finite domain, and the walls of the channel result in additional drag forces on the particles due to hydrodynamic interaction [12,74]. The effect of this drag is about 42% of the simple Stokes drag, when a 12.32 μm bead is in the mid-plane of a 40 μm shallow channel [12]. The correction may be larger if the bead is off-centre and closer to the channel wall. This will result in an overestimation of E_{ac} by the least-squares method, and the experimental results in Fig. 8 would be shifted further away from theoretical prediction. The additional drag due to the surfaces results in a smaller normalised interparticle radiation force, $F_{2,x}^{(1)}/(E_{ac}k^4a^6)$ being obtained from experiments. In Ref. [12] it was shown that the decrease in experimental result, $F_{2,x}^{(1)}/(E_{ac}k^4a^6)$, will be about 18% between two 12.32 μm beads separated at $r/a = 2.26$, when the beads are at the mid-plane between top and bottom surfaces . Nevertheless, the difference between theoretical and experimental results of interparticle radiation forces will decrease with the inclusion of wall effects.

4   Predicting cluster patterns

To study the clustering patterns in an acoustic field, it is important to consider the collision behavior of the objects. The position correction method [21] and the collision tracking model [10] can be used to investigate the clustering patterns for a given external field. In Fig. 9 identical spheres undergo close-range agglomeration within the pressure node of a plane standing wave with zero primary radiation force. The spheres are located initially on the nodal plane resulting in zero primary force throughout the simulation. This is to investigate their dynamics under only the interaction forces. The position correction method is illustrated in Fig. 9(a) and (b) for the cases of two and three solid spheres, respectively, to ensure that the no-penetration condition is met throughout the clustering process. A pair attracts each other directly along the centre-to-centre line, as shown in Fig. 9(c). The effects of rotational coupling become apparent when there are more than two objects, as shown in Fig. 9(d)-(f) for three, six and ten spheres, resulting in a collective rotation with the direction depending on the shape of the cluster. The evolution of acoustical agglomeration under the action of radiation and hydrodynamic forces can be tracked by using time-adaptive approaches, which are outlined in references [10,21], for the quasi-static regime of sub-wavelength particles in an acoustic field.

5   Effects of viscosity on interaction force

It is well-known that the viscosity triggers acoustic streaming, an additional time-averaged flow induced by the attenuation of outgoing waves [24,25]. Strong streaming effects in a fluid cavity occur due to walls. The contribution from the particles' scattering to the streaming flow, which is also referred to as microstreaming, may become comparable to or overcome the wall-induced streaming, depending on the ratio of the material properties of the particles and the fluid [28,84]. Studies on the effects of viscosity on acoustic interaction forces showed an increase of radial attraction/repulsion due to the fluid streaming around a pair of particles, assuming a free-space fluid domain [20]. This means the effects of acoustic streaming, originating either from the side walls or the particles, can be accounted for as an additional hydrodynamic resistance force. In the experimental measurements of acoustic interaction force, it is necessary to consider that the total hydrodynamic forces are induced by a background flow, acoustic streaming generated by channel walls, and the motion of
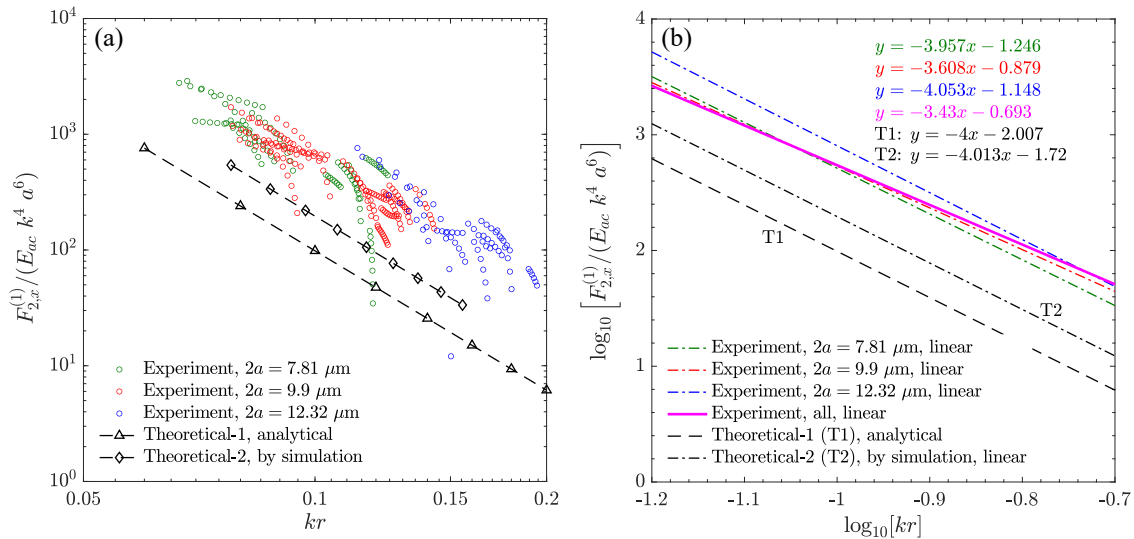
Fig. 8 Comparison between experimentally measured and theoretical interaction force. (a) Experimental and theoretical interaction force across three different sizes of beads[12]. (b) Linear fit of the experimental observations and Theoretical-2, by simulation. Theoretical-1 is from the analytical formula by Silva and Bruus (2014)[83]. Theoretical-2 is from the numerical simulation similar to Sepehrirahnama *et al.* (2015)[7]. Reprinted figure with permission from Mohapatra A. R., Sepehrirahnama S., Lim K.-M., Physical Review E, 97, 053105, 2018. Copyright (2018) by the American Physical Society. http://dx.doi.org/10.1103/PhysRevE.97.053105.
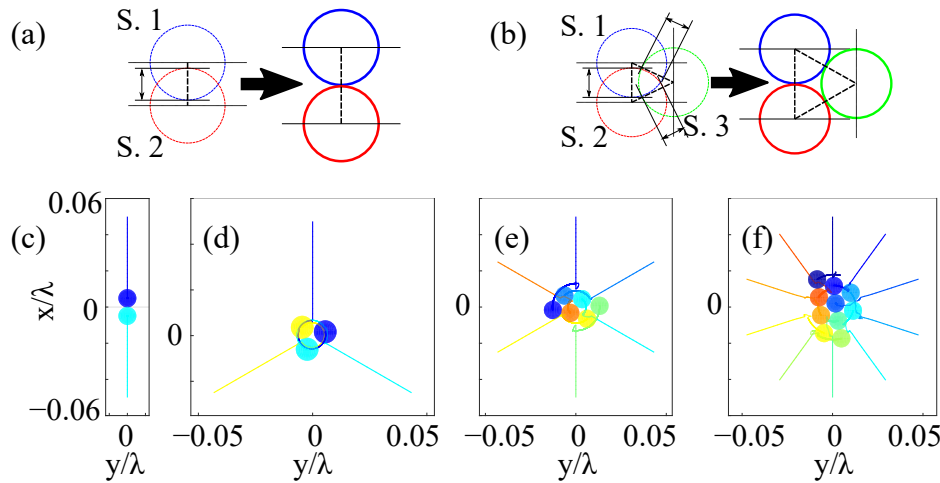

Fig. 9 Schematics of collision detection and position adjustment for (a) two and (b) three non-penetrating spherical objects in the close-range regime of acoustic interaction. Trajectories and cluster formation of (c) two, (d) three, (e) six and (f) ten rigid spheres, with $ka \approx 0.03$ corresponding to 5 μm particles subject to a frequency of 1.5 MHz in an ideal fluid, are shown in the pressure node of a plane standing wave with zero primary radiation force. Reprinted by permission from Springer Nature Customer Service Centre GmbH: SpringerLink, Microfluidics and Nanofluidics, Acoustophoretic agglomeration patterns of particulate phase in a host fluid. Sepehrirahnama, S., Lim, KM. (2020), advance online publication, 2 November 2020, https://doi.org/10.1007/s10404-020-02397-5

surrounding particles. At large distances from the walls, hydrodynamic interaction between the objects and the walls becomes negligible. Nevertheless, the accuracy of the measured energy density and interaction force depends on the inclusion of these hydrodynamic effects into the particle dynamics model.

Viscosity of the fluid medium affects the scattering response of particles and objects, even in the Rayleigh limit of $ka \ll 1$, by dissipating acoustic energy[13,20,26]. In addition, this viscous dissipation leads to a second-order effect in the form of a time-averaged flow that is called acoustic streaming[24,25]. To formulate the effects of viscosity on the acoustic interaction force, we start by revisiting the governing equations. For a compressible and vis-

cous fluid and in the absence of body forces, the Navier-Stokes equations become[13],

$$\partial_t \overline{\rho} + \boldsymbol{\nabla} \cdot (\overline{\rho}\overline{\mathbf{v}}) = 0,$$

$$\partial_t (\overline{\rho}\overline{\mathbf{v}}) + \boldsymbol{\nabla} \cdot (\overline{\rho}\overline{\mathbf{v}}\overline{\mathbf{v}}) = -\boldsymbol{\nabla}\overline{p} + \mu\nabla^2\overline{\mathbf{v}} + \left(\eta + \frac{1}{3}\mu\right)\boldsymbol{\nabla}(\boldsymbol{\nabla} \cdot \overline{\mathbf{v}}),$$

(41)

where μ and η denote the shear and bulk viscosity coefficients. Substituting the perturbation expansion of the pressure, velocity and density fields Eq. (2) into Eq. (41) and keeping the first-order

terms, the acoustic wave equation for a viscous fluid becomes [19]

$$\partial_t \rho = -\rho_f \boldsymbol{\nabla} \cdot \mathbf{v},$$

$$\rho_f \partial_t \mathbf{v} = -\boldsymbol{\nabla} \overline{p} + \mu \nabla^2 \mathbf{v} + \left(\eta + \frac{1}{3}\mu\right)\boldsymbol{\nabla}(\boldsymbol{\nabla} \cdot \mathbf{v}). \qquad (42)$$

By using the Helmholtz decomposition of the acoustic velocity field $\mathbf{v} = \nabla\phi + \nabla \times \boldsymbol{\Psi}$ under the gauge condition $\boldsymbol{\nabla} \cdot \boldsymbol{\Psi} = 0$ and the fluid equation of state $p = c_f^2 \rho$, the acoustic wave propagation can be further described using a scalar and a vector wave equations as

$$(\nabla^2 + k^2)p = 0, \qquad k = \frac{\omega}{c_f}\left(1 - \frac{i\omega}{\rho_f c_f^2}\left[\frac{4}{3}\mu + \eta\right]\right)$$

$$(\nabla^2 + k_\mu^2 \boldsymbol{\Psi}) = \mathbf{0}, \qquad k_\mu = \frac{1+i}{\delta} = (1+i)\sqrt{\frac{2\mu}{\rho_f \omega}} \qquad (43)$$

$$p = -\rho_f \partial_t \phi.$$

where k and k_μ denote the wavenumbers of the pressure and shear waves, respectively, $\delta = \sqrt{2\mu/(\omega\rho_f)}$ is the viscous penetration depth, also known as the acoustic boundary layer thickness, and $\nabla^2\boldsymbol{\Psi} = \boldsymbol{\nabla} \times (\boldsymbol{\nabla} \times \boldsymbol{\Psi})$. The complex wavenumbers in Eq. (43) imply the acoustic energy dissipation in both the pressure and shear waves. It is expected that viscous dissipation changes the scattering strengths of objects compared to case of an ideal fluid. To understand the change in the acoustic radiation force, the governing equations of acoustic streaming are revisited. By substituting Eq. (2) into Eq. (41), keeping the second-order terms only, and time-averaging, the acoustic streaming equations become

$$\rho_f \boldsymbol{\nabla} \cdot \langle \tilde{\mathbf{v}} \rangle = m_b, \qquad m_b = -\boldsymbol{\nabla} \cdot \langle \rho \mathbf{v} \rangle$$

$$-\boldsymbol{\nabla}\langle \tilde{\boldsymbol{\sigma}} \rangle = \mathbf{f}_b, \qquad \mathbf{f}_b = -\langle \rho \partial_t \mathbf{v} \rangle - \rho_f \langle (\mathbf{v} \cdot \boldsymbol{\nabla})\mathbf{v} \rangle, \qquad (44)$$

$$\tilde{\boldsymbol{\sigma}} = -\tilde{p}\mathbf{I} + \mu\left(\boldsymbol{\nabla}\tilde{\mathbf{v}} + [\boldsymbol{\nabla}\tilde{\mathbf{v}}]^T\right) + \left(\eta - \frac{2}{3}\mu\right)\boldsymbol{\nabla} \cdot \tilde{\mathbf{v}},$$

where superscript T denotes the tensor transpose operator. Compared to streaming in an ideal fluid Eq. (7), the volumetric mass m_b and force $\mathbf{f}_b$ terms are unchanged; however, the viscous stresses are included in the momentum conservation equation. This implies that acoustic streaming induces hydrodynamic effects due to viscous stresses. Hence, similar to Eq. (9) and using Eq. (12), the mean force acting on objects, being the sum of the radiation forces and the hydrodynamic streaming force, is

$$\mathbf{F} = \int_\Gamma \langle \tilde{\boldsymbol{\sigma}} - \rho_f \mathbf{v}\mathbf{v} \rangle \cdot \mathbf{n} d\Gamma. \qquad (45)$$

Equation (44) describes fluid motion under volumetric source terms m_b and $\mathbf{f}_b$, which are quadratic functions of the acoustic density and velocity fields. To solve Eq. (44) for streaming associated with the scattered acoustic fields, the self-product of the external acoustic fields, i.e., $\langle \rho_0 \mathbf{v}_0 \rangle$, $\langle \rho_0 \partial_t \mathbf{v}_0 \rangle$, and $\langle (\mathbf{v}_0 \cdot \boldsymbol{\nabla})\mathbf{v}_0 \rangle$, are subtracted from the source terms m_b and $\mathbf{f}_b$ [13,20,26,27]. Using Eq. (18), an example of this deviatoric form of the scalar source

term $m_b^{(s)}$ is given in the following,

$$m_b^{(s)} = -\boldsymbol{\nabla} \cdot \langle \rho\mathbf{v} - \rho_0\mathbf{v}_0 \rangle$$

$$= -\boldsymbol{\nabla} \cdot \left\langle \rho_0 \sum_{n;q}\mathbf{v}_n + \sum_{n;q}\rho_n\mathbf{v}_0 + \sum_{n;q}\rho_n\sum_{n;q}\mathbf{v}_n + \right. \qquad (46)$$

$$\left. \hat{\rho}_q\mathbf{v}_q + \hat{\mathbf{v}}_q\rho_q + \rho_q\mathbf{v}_q \right\rangle,$$

where $m_b^{(s)}$ denotes the scattering-dependant scalar source. Similarly, we can obtain the expression of the deviatoric vector source term $\mathbf{f}_b^{(s)}$ using $\langle \rho\partial_t\mathbf{v} - \rho_0\partial_t\mathbf{v}_0 \rangle$ and $\langle (\mathbf{v} \cdot \boldsymbol{\nabla})\mathbf{v} - (\mathbf{v}_0 \cdot \boldsymbol{\nabla})\mathbf{v}_0 \rangle$. Using the divergence theorem and Eq. (44), the contribution from products of the external fields become zero and the mean force in Eq. (45) becomes

$$\mathbf{F} = \int_\Gamma \langle \tilde{\boldsymbol{\sigma}}^{(s)} - \rho_f(\mathbf{v}\mathbf{v})^{(s)} \rangle \cdot \mathbf{n} d\Gamma, \qquad (47)$$

where superscript (s) denotes the deviatoric form of the product terms, similar to Eq. (46).

Similar to the case of an ideal fluid, we need to solve the multiple scattering problem in an infinite domain neglecting the wall-induced streaming. The boundary condition of the tangential component of the acoustic velocity should be accounted for in the boundary conditions for the case of viscous fluid, and Eq. (31) becomes

$$\hat{\mathbf{v}}_q \cdot \mathbf{n}_q + \mathbf{v}_q \cdot \mathbf{n}_q = \overline{\mathbf{v}}_q \cdot \mathbf{n}_q + \mathbf{u}_q \cdot \mathbf{n}_q,$$

$$\hat{\mathbf{v}}_q \cdot \mathbf{t}_q + \mathbf{v}_q \cdot \mathbf{t}_q = \overline{\mathbf{v}}_q \cdot \mathbf{t}_q + \mathbf{u}_q \cdot \mathbf{t}_q,$$

$$\hat{p}_q + p_q = \overline{p}_q, \qquad (48)$$

$$\mathbf{u}_q = \frac{i}{\rho_q\Omega_q\omega}\int_{\Gamma_q}(\hat{p}_q + p_q)\mathbf{n}_q d\Gamma,$$

where $\mathbf{t}_q$ is the unit tangent vector to the surface of particle q, which can be decomposed into two orthogonal components in a given coordinate system. The acoustic boundary conditions Eq. (48) can be solved numerically, e.g., by a Finite Element model of acoustic scattering in a lossy fluid [28] or using a multipole expansion of velocity potentials and the orthogonality of the spherical harmonics describing the angular dependence of the fields [20,27]. Without loss of generality, we consider an axisymmetric configuration of a pair spherical particles on the opposite sides of a pressure node of a plane standing wave, i.e. the external field has no vector velocity potential component, $\boldsymbol{\Psi}_0 = \mathbf{0}$ and $\mathbf{v}_0 = \boldsymbol{\nabla}\phi_0$. The scalar velocity potential is expressed as in Eq. (30) for an ideal fluid, with scattering coefficients $B_{n0}^{(q)}$. The vector velocity potential $\boldsymbol{\Psi}$ becomes

$$\boldsymbol{\Psi} = \boldsymbol{\Psi}_1 + \boldsymbol{\Psi}_2$$

$$\boldsymbol{\Psi}_q = e^{-i\omega t}\mathbf{e}_\varphi^{(q)}\sum_{l=0}^\infty D_N^{(q)}h_n(k_\mu r_q)\frac{dY_{l0}}{d\theta_q}, \qquad q = 1, 2 \qquad (49)$$

where $(r_q, \theta_q, \varphi_q)$ denote the spherical coordinates with respect to the local coordinate system at the origin of sphere q, and Y_{l0} is the spherical harmonics of degree zero, i.e., $m = 0$, indicating

the axisymmetry of this problem. Since the vector velocity potential $\boldsymbol{\Psi}$ has only one component in the azimuthal φ direction, it generates acoustic velocity components in the radial direction r and polar polar direction θ. Hence, for this case of a pair of rigid immovable spheres in an axisymmetric configuration, and using the orthogonality of the spherical harmonics, the boundary conditions become

$$\int_{\Gamma_q} Y_{l0}\left(\mathbf{v}_q \cdot \mathbf{n}_q + \mathbf{v}_{3-q} \cdot \mathbf{n}_q\right) d\Gamma_q = \int_{\Gamma_q} Y_{l0}\left(\mathbf{v}_0 \cdot \mathbf{n}_q\right) d\Gamma_q$$

$$\int_{\Gamma_q} \frac{dY_{l0}}{d\theta_q}\left(\mathbf{v}_q \cdot \mathbf{t}_q + \mathbf{v}_{3-q} \cdot \mathbf{t}_q\right) d\Gamma_q = \int_{\Gamma_q} \frac{dY_{l0}}{d\theta_q}\left(\mathbf{v}_0 \cdot \mathbf{t}_q\right) d\Gamma_q, \tag{50}$$

where $q = 1,2$ giving four independent sets of equations from which the scattering coefficients $B_{n0}^{(1)}$, $D_{n0}^{(1)}$, $B_{n0}^{(2)}$ and $D_{n0}^{(2)}$ are obtained[20], for up to a given cut-off order. The cut-off order can be $l = 3$ and $l = 6$ for large and small interparticle distances, respectively. The minimum cut-off order can be obtained from a convergence analysis of the scattered pressure field or of the resultant acoustic radiation force[20].

Next, the source terms m_b and $\mathbf{f}_b$ in the streaming equations, Eq. (44), are obtained from the external and scattered pressure and velocity fields. The effects of the scalar source term m_b are negligible compared to those of the vector source term $\mathbf{f}_b$[13,20,26,27,55]; hence, m_b can be set to zero and the streaming flow becomes an incompressible linear Stokes flow[20,26,27]. The streaming pressure $\tilde{p}$ and velocity $\tilde{\mathbf{v}}$ in Eq. (44) can be solved using numerical models of inhomogeneous Stokes flow, e.g. using the Microfluidic module in the COMSOL Multiphysics software package, or the method of Stokeslet[85], which is similar to partial wave expansion for acoustic scattering. The pair of spheres responds to the source terms m_b and $\mathbf{f}_b$ by generating an additional streaming flow such that the boundary conditions, e.g. no-slip condition, are met at their surfaces. The method of Stokeslet as a well established analytical solution of linear viscous flow[85] which can be implemented by discretizing the body of the fluid into small volume elements, placing a Stokeslet at their centroids, and calculating the effects of each fluid element on the surface of the spheres. The method of Stokeslet for a pair of spheres can be written as

$$\langle\tilde{\mathbf{v}}\rangle = \langle\tilde{\mathbf{v}}\rangle_1 + \langle\tilde{\mathbf{v}}\rangle_2 + \langle\tilde{\mathbf{v}}\rangle^{(S)}$$

$$\langle\tilde{p}\rangle = \langle\tilde{p}\rangle_1 + \langle\tilde{p}\rangle_2 + \langle\tilde{p}\rangle^{(S)}$$

$$\langle\tilde{\mathbf{v}}\rangle_{\mathbf{x}_o}^{(S)} = \sum_{l=1}^{N} \frac{\Omega_n}{8\pi\mu}\left(\frac{\mathbf{I}}{r_n} + \frac{\mathbf{r}_n\mathbf{r}_n}{r_N^3}\right)\mathbf{f}_b^{(n)},$$

$$\langle\tilde{p}\rangle_{\mathbf{x}_o}^{(S)} = \sum_{l=1}^{N} \frac{\Omega_n}{4\pi}\frac{\mathbf{r}_n}{r_n^3}\cdot\mathbf{f}_b^{(n)}, \tag{51}$$

$$\mathbf{r}_n = \mathbf{x}_n - \mathbf{x}_o, \qquad r_n^2 = \mathbf{r}_n \cdot \mathbf{r}_n,$$

where Ω_n denotes the volume of the nth fluid element, $\mathbf{f}_b^{(n)}$ is the vector source term evaluated at the centroid of element n, and $\mathbf{x}_o$ denotes the position vector of the probe point. This implementation requires a cut-off size for the fluid domain, e.g., larger than

5λ away from the smallest surface enclosing all particles, to generate a finite computational domain representing the infinite free space fluid domain[20].

The contributions of sphere q to the streaming flow are denoted by $\langle\tilde{\mathbf{v}}_q\rangle$ and $\langle\tilde{p}_q\rangle$, and can be expressed using a set of scalar and vector potential functions[13,20,27]

$$\langle\tilde{\mathbf{v}}_q\rangle = \boldsymbol{\nabla}\tilde{\phi}_q + \boldsymbol{\nabla}\times\tilde{\boldsymbol{\psi}}_q,$$

$$\langle\tilde{p}_q\rangle = \mu\nabla^2\boldsymbol{\nabla}\times\tilde{\boldsymbol{\psi}}_q. \tag{52}$$

These potentials can be written in terms of a multipole expansion in the $k = 0$ limit[13] as

$$\tilde{\phi}_q = \sum_{l=0}^{\infty} \tilde{B}_n^{(q)}\left(\frac{a_q}{r_q}\right)^{n+1} Y_{l0},$$

$$\tilde{\boldsymbol{\psi}}_q = \mathbf{e}_\varphi^{(q)} \sum_{l=0}^{\infty} \frac{\tilde{D}_n^{(q)}}{4n-2}\left(\frac{a_q}{r_q}\right)^{n-1}\frac{dY_{l0}}{d\theta_q} \tag{53}$$

where a_q is the radius of sphere q. The set of coefficients $\tilde{B}_n^{(q)}$ and $\tilde{D}_n^{(q)}$ are obtained from the boundary conditions for the streaming flow on the spheres, which are written using the orthogonality of spherical harmonics as

$$\int_{\Gamma_q} Y_{l0}\left(\langle\tilde{\mathbf{v}}\rangle_q \cdot \mathbf{n}_q + \langle\tilde{\mathbf{v}}\rangle_{3-q}\cdot\mathbf{n}_q\right)d\Gamma_q = \int_{\Gamma_q} Y_{l0}\left(\langle\tilde{\mathbf{v}}\rangle^{(S)}\cdot\mathbf{n}_q\right)d\Gamma_q$$

$$\int_{\Gamma_q} \frac{dY_{l0}}{d\theta_q}\left(\langle\tilde{\mathbf{v}}\rangle_q \cdot \mathbf{t}_q + \langle\tilde{\mathbf{v}}\rangle_{3-q}\cdot\mathbf{t}_q\right)d\Gamma_q = \int_{\Gamma_q} \frac{dY_{l0}}{d\theta_q}\left(\langle\tilde{\mathbf{v}}\rangle^{(S)}\cdot\mathbf{t}_q\right)d\Gamma_q, \tag{54}$$

where $q = 1,2$. From $\tilde{B}_n^{(q)}$ and $\tilde{D}_n^{(q)}$, the streaming pressure and velocity, and subsequently, stresses are calculated using Eq. (44), and Eqs. (51)-(53).

For object q, the total force in Eq. (47) can be split into partial forces of radiation and streaming (hydrodynamic) types as

$$\mathbf{F}^{(q)} = \mathbf{F}_0^{(q)} + \sum_{n;q}\mathbf{F}_n^{(q)} + \mathbf{H}^{(q)}, \tag{55}$$

where $\mathbf{F}_0^{(q)}$ and $\mathbf{F}_n^{(q)}$ are the primary and interparticle radiation forces, respectively, and $\mathbf{H}^{(q)}$ denotes the hydrodynamic force, including hydrodynamic interaction effects. For a single sphere, it has been shown that $\mathbf{H}^{(q)}$ reduces to the Stokes drag[13,85], and $\mathbf{F}^{(q)}$ is the sum of the primary radiation force and the Stokes drag. However, this separation of the interaction force due to radiation from the hydrodynamic interaction is yet to be done, and the Stokeslet method can be integrated into the force potential formulation Sec. 2.3 to realize this distinction. To demonstrate the effects of viscosity on the radiation force, the combined radiation and hydrodynamic interaction forces can be obtained as

$$\mathbf{F}_{\text{int}}^{(q)} = \sum_{n;q}\mathbf{F}_n^{(q)} + \mathbf{H}^{(q)} = \mathbf{F}^{(q)} - \mathbf{F}_0^{(q)}, \tag{56}$$

where $\mathbf{F}^{(q)}$ is obtained by solving for the streaming pressure, velocity and stresses in Eq. (44), using Eqs. (50), (46), (51) and (54), and substituting them into Eq. (47). The primary radiation

force $\mathbf{F}_0^{(q)}$ can be obtained from the far-field approach Eq. (21), as described in [19] for particles with size in the Rayleigh limit $ka \ll 1$, or using the series expansion of $\mathbf{F}^{(q)}$ in Eq. (32) [20,27,86], for which the scattering coefficients are obtained by assuming that particle q is alone in the fluid domain.

The effects of viscosity on the interaction force are shown in Fig. 10, for a pair of spheres at the two sides of a pressure node of a plane standing wave, as shown in Fig. 10(f). In this symmetric configuration, all force components acting on the spheres are equal in magnitude and opposite in direction. Spheres of radius 1, 5, and 10 μm are considered while the wavelength is 1 mm, e.g., water at room temperature and wave frequency of 1.5 MHz [2,54,87], corresponding to viscous penetration depth $\delta = 0.4$ μm. In Fig. 10(a), it is shown that the primary forces calculated for both cases of a single sphere and a pair of spheres match well, with relative difference of less than 1% for a wide range of interparticle distance d, in which the total force decreases by at least three orders of magnitude, as shown in Fig. 10(b). Furthermore, in Fig. 10(b), the total force with and without viscosity, i.e., obtained from Eq. (47) and Eq. (20), respectively, are shown to differ by order of several magnitude for small separation d. Viscosity effects become negligible when particles are relatively far apart $d/\delta > 210$. The interaction force $\mathbf{F}_{\text{int}}$ calculated using Eq. (56) is shown in Fig. 10(c)-(e) for three sizes of spheres, and compared against calculations with no viscosity from Eq. (34). Also, a third case, in which the interaction force is obtained by including the viscosity effects on the scattering fields (first-order effects) in Eq. (34) and without considering the streaming flow (second-order effects), is shown in Fig. 10(c)-(e) to demonstrate the significant hydrodynamic role of streaming in the increase of the interaction forces by several orders of magnitude. Finally, it is shown in Fig. 10(g)-(h) that the interaction force $\mathbf{F}_{\text{int}}$ reduces by approximately 20% when the dynamic viscosity μ is reduced to 0.2%, i.e., $\mu/500$, confirming that the viscosity value has less direct influence on the interaction force, and its indirect effect of inducing streaming flow is more significant.

This theoretical study of viscosity effects on the interaction force provides insights into the role of streaming flow and the dependence on the dynamic viscosity of a host fluid. However, this area is yet to be fully explored, as it might be possible to separate out the radiation and hydrodynamic components of the interaction force using the methodology in Sec. 2.3 or the approach based on Finite Element Multiphysics [84]. This entails separating the interaction-related terms, similar to Eq. (18), in the expressions of the source terms m_b and $\mathbf{f}_b$ in Eq. (44) and applying the far-field approach to obtain the radiation-related interaction force from Eq. (32) and the estimate of the primary radiation force.

6 Conclusion

In this Tutorial, the principles of acoustic interaction force were presented, for both cases of fluid with and without viscosity. Main features of this force was shown using the modelling results and their roles in clustering patterns was demonstrated. Experimental caluclations of the interaction force were provided to investigate the validity of the theoretical models.

Theoretical models of acoustic interaction were presented to demonstrate its dependence on factors including object size, compressibility, incident wavelength and fluid viscosity, and to provide benchmark cases with a pair of spherical particles as reference. The first model based on force potential analysis led to explicit expressions for the interaction forces and force potentials. The second model based on the Partial-Wave expansion provided a series expression for the total and primary radiation forces, and the interaction force was obtained from their difference. Using these models, the coupled-rotation and non-reciprocity features were explained as the distinguishing features of acoustic interaction. A numerical model, verified against the analytical results, was developed and it is made available as Supplementary Material for the readers.

The challenges of experimental measurements such as estimation of energy density and indirect extraction of acoustic interaction forces from a hydrodynamic model were discussed. A comparison between theoretical and experimental results of these forces was presented. It was concluded that describing the clustering of objects under an external acoustic field requires a pairwise analysis of interactions and a model of collision detection depending on the object types in a mixture. Considering the rotational coupling and non-reciprocity of the interaction forces, the close-range clustering patterns are far more complicated [23] than the typical notion of repulsion-attraction, originating from the concept of electrostatic interaction. It is envisaged that future research on acoustic interaction will lead to the improvement of theoretical models and, more importantly, to the development of novel applications for customised manipulation based on small clusters. In the longer term, understanding and controlling acoustic interaction forces and torques could provide a novel approach for combining the field of sub-wavelength acoustic metamaterials and acoustophoresis. Potential applications include localized beam manipulation and trapping, hierarchical sorting by inducing enhanced clustering between similar objects, and multiscale acoustophoresis through controlling nano-sized objects with micron-sized objects.

Author contributions

Shahrokh Sepehrirahnama: Conceptualization, Methodology, Software, Validation, Formal analysis, Investigation, Data Curation, Writing - Original Draft, Writing - Review & Editing, Visualization, Project administration **Abhishek Ray Mohapatra**: Conceptualization, Methodology, Software, Validation, Formal analysis, Investigation, Data Curation, Writing - Original Draft, Writing - Review & Editing, Visualization. **Sebastian Oberst**: Writing - Review & Editing, Supervision, Project administration, Funding Acquisition. **Yan Kei Chiang**: Methodology, Software, Validation, Formal analysis, Investigation, Data Curation, Writing - Original Draft, Writing - Review & Editing. **David A. Powell**: Writing - Review & Editing, Supervision, Funding Acquisition. **Kian-Meng Lim**: Conceptualization, Writing - Original Draft, Writing - Review & Editing, Supervision, Funding Acquisition.

Acknowledgement
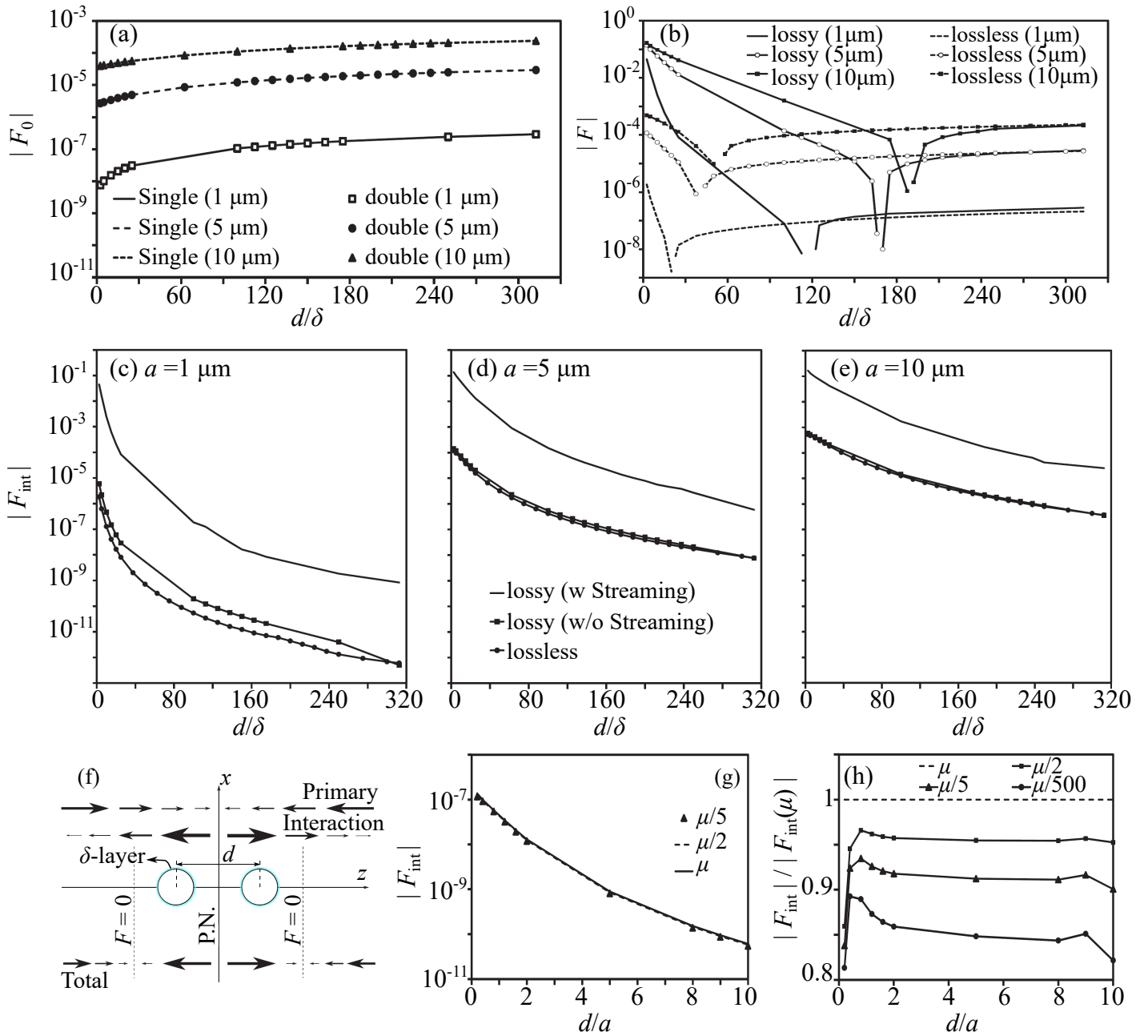
Lab on a Chip Accepted Manuscript

Fig. 10 Effects of viscosity on the primary radiation force, mean acoustic force obtained from Eq. (47), and the interaction force using Eq. (56), for the symmetric configuration of a pair of spheres around a pressure node in a standing wave, as shown in panel (f). Due to the symmetric configuration, forces on each sphere are equal in magnitude, opposite in direction and act only in the z-direction, so only their absolute values are reported. Panel (a) shows the primary force acting on a sphere when it is isolated and when it is paired with another. Panel (b) shows the total force acting on spheres of size 1, 5, and 10 μm for the cases of viscous fluid (lossy) and ideal fluid (lossless). Panels (c)-(e) shows the acoustic interaction force for three different scenarios, i.e., a viscous fluid with streaming (solid line), a viscous fluid without considering streaming (line with square markers), and an ideal fluid. In all the cases, the interaction force is obtained from the difference between the total force $\mathbf{F}$ and primary radiation force $\mathbf{F}_0$. Panel (f) demonstrate schematically the directions of the total, primary and interaction forces and the size of the viscous penetration layer (δ-layer) compared to the radius and the distance from the pressure node $d/2$. The locations where the interaction force balances out the primary radiation force are marked by total force being zero, $F = 0$. Panels (g) and (h) show the changes of the interaction force with respect to different values of dynamic viscosity μ, in the absolute and relative form, respectively, for sphere size of $a = 5$ μm. Reprinted figure with permission from Sepehrirahnama, S., Chau, F. S., and Lim K.-M., Physical Review E, 93 (2), 023307, 2016. Copyright (2016) by the American Physical Society. `http://dx.doi.org/10.1103/PhysRevE.93.023307`.

Conflicts of interest

There are no conflicts to declare.

Notes and references

1 H. Bruus, Lab on a Chip, 2011, **11**, 3742–3751.

2 H. Bruus, Lab on a Chip, 2012, **12**, 1014–1021.

3 J. Dual, P. Hahn, I. Leibacher, D. Möller, T. Schwarz and J. Wang, Lab on a Chip, 2012, **12**, 4010–4021.

4 X. Zheng and R. E. Apfel, The Journal of the Acoustical Society of America, 1995, **97**, 2218–2226.

5 A. A. Doinikov, Journal of Fluid Mechanics, 2001, **444**, 1–21.

6 G. T. Silva and H. Bruus, Physical Review E, 2014, **90**, 063007.

7 S. Sepehrirahnama, K.-M. Lim and F. S. Chau, The Journal of the Acoustical Society of America, 2015, **137**, 2614–2622.

8 J. H. Lopes, M. Azarpeyvand and G. T. Silva, IEEE transactions on ultrasonics, ferroelectrics, and frequency control, 2016, **63**, 186–197.

9 A. Garcia-Sabaté, A. Castro, M. Hoyos and R. González-Cinca, The Journal of the Acoustical Society of America, 2014, **135**, 1056–1063.

10 T. Baasch, I. Leibacher and J. Dual, The Journal of the Acoustical Society of America, 2017, **141**, 1664–1674.

11 F. B. Wijaya, S. Sepehrirahnama and K.-M. Lim, Wave Motion, 2018, **81**, 28–45.

12 A. R. Mohapatra, S. Sepehrirahnama and K.-M. Lim, Physical Review E, 2018, **97**, 053105.

13 A. Doinikov, Proceedings of the Royal Society of London. Series A: Mathematical and Physical Sciences, 1994, **447**, 447–466.

14 A. A. Doinikov, The Journal of the Acoustical Society of America, 1998, **103**, 143–147.

15 S. Sepehrirahnama and K.-M. Lim, Physical Review E, 2020, **102**, 043307.

16 L. A. Crum, The Journal of the Acoustical Society of America, 1975, **57**, 1363–1370.

17 F. Mitri, Ultrasonics, 2006, **44**, 244–258.

18 S. Sepehrirahnama, S. Oberst, Y. Chiang and D. Powell, Physical Review E, 2021, **104**, 065003.

19 M. Settnes and H. Bruus, Physical Review E, 2012, **85**, 016327.

20 S. Sepehrirahnama, F. S. Chau and K.-M. Lim, Physical Review E, 2016, **93**, 023307.

21 S. Sepehrirahnama and K.-M. Lim, Microfluidics and Nanofluidics, 2020, **24**, 1–14.

22 M. Evander and J. Nilsson, Lab on a Chip, 2012, **12**, 4667–4676.

23 M. X. Lim, A. Souslov, V. Vitelli and H. M. Jaeger, Nature Physics, 2019, **15**, 460–464.

24 S. Sadhal, Lab on a Chip, 2012, **12**, 2292–2300.

25 S. Sadhal, Lab on a Chip, 2012, **12**, 2600–2611.

26 S. Sepehrirahnama, K.-M. Lim and F. S. Chau, Physics Procedia, 2015, **70**, 80–84.

27 S. Sepehrirahnama, F. S. Chau and K.-M. Lim, Physical Review E, 2015, **92**, 063309.

28 T. Baasch, A. Pavlic and J. Dual, Physical Review E, 2019, **100**, 061102.

29 T. Embleton, The Journal of the Acoustical Society of America, 1962, **34**, 1714–1720.

30 T. Leighton, A. Walton and M. Pickworth, European Journal of Physics, 1990, **11**, 47.

31 T. Barbat, N. Ashgriz and C.-S. Liu, Journal of Fluid Mechanics, 1999, **389**, 137–168.

32 J. Jiao, Y. He, S. E. Kentish, M. Ashokkumar, R. Manasseh and J. Lee, Ultrasonics, 2015, **58**, 35–42.

33 A. A. Doinikov, Physical Review E, 1999, **59**, 3016.

34 N. A. Pelekasis, A. Gaki, A. Doinikov and J. A. Tsamopoulos, Journal of Fluid Mechanics, 2004, **500**, 313–347.

35 K. Yoshida, T. Fujikawa and Y. Watanabe, The Journal of the Acoustical Society of America, 2011, **130**, 135–144.

36 F. Dzaharudin, S. A. Suslov, R. Manasseh and A. Ooi, The Journal of the Acoustical Society of America, 2013, **134**, 3425–3434.

37 M. Weiser, R. Apfel and E. Neppiras, Acta Acustica united with Acustica, 1984, **56**, 114–119.

38 F. B. Wijaya, A. R. Mohapatra, S. Sepehrirahnama and K.-M. Lim, Microfluidics and Nanofluidics, 2016, **20**, 69.

39 G. Regnault, C. Mauger, P. Blanc-Benon and C. Inserra, Physical Review E, 2020, **102**, 031101.

40 S. Z. Hoque and A. K. Sen, Physics of Fluids, 2020, **32**, 072004.

41 M. X. Lim, B. VanSaders, A. Souslov and H. M. Jaeger, Physical Review X, 2022, **12**, 021017.

42 J. P. Armstrong, S. A. Maynard, I. J. Pence, A. C. Franklin, B. W. Drinkwater and M. M. Stevens, Lab on a Chip, 2019, **19**, 562–573.

43 D. Bazou, W. T. Coakley, K. M. Meek, M. Yang and D. T. Pham, Colloids and Surfaces A: Physicochemical and Engineering Aspects, 2004, **243**, 97–104.

44 M. Gröschl, Acustica, 1998, **84**, 432–447.

45 B. Hammarström, T. Laurell and J. Nilsson, Lab on a Chip, 2012, **12**, 4296–4304.

46 M. Wu, J. Rufo, Z. Wang, R. Fang and T. J. Huang, Microsystems & Nanoengineering, 2019, **5**, 32.

47 R. Habibi, C. Devendran and A. Neild, Lab on a Chip, 2017, **17**, 3279–3290.

48 G. T. Silva, J. H. Lopes, J. P. Leão-Neto, M. K. Nichols and B. W. Drinkwater, Physical Review Applied, 2019, **11**, 054044.

49 D. Saeidi, M. Saghafian, S. Haghjooy Javanmard and M. Wiklund, Micromachines, 2020, **11**, 152.

50 R. Barnkob, P. Augustsson, T. Laurell and H. Bruus, Physical Review E, 2012, **86**, 056307.

51 K. Xu, C. P. Clark, B. L. Poe, J. A. Lounsbury, J. Nilsson, T. Laurell and J. P. Landers, Analytical chemistry, 2019, **91**, 2186–2191.

52 C. P. Clark, K. Xu, O. Scott, J. Hickey, A.-C. Tsuei, K. Jackson

and J. P. Landers, Forensic Science International: Genetics, 2019, **41**, 42–49.

53 H. D. A. Santos, A. E. Silva, G. C. Silva, E. B. Lima, A. S. Marques, M. S. Alexandre-Moreira, A. C. Queiroz, C. Jacinto, J. Henrique Lopes, U. Rocha and G. T. Silva, Advanced Engineering Materials, 2021, **23**, 2100552.

54 H. Bruus, Lab on a Chip, 2012, **12**, 20–28.

55 S. Sepehrirahnama, PhD Dissertation, National University of Singapore, 2015.

56 K. Yosioka and Y. Kawasima, Acta Acustica united with Acustica, 1955, **5**, 167–173.

57 G. Simon, M. A. B. Andrade, M. P. Y. Desmulliez, M. O. Riehle and A. L. Bernassau, Micromachines, 2019, **10**, 431.

58 P. Mishra, M. Hill and P. Glynne-Jones, Biomicrofluidics, 2014, **8**, 034109.

59 A. Doinikov and S. Zavtrak, Physics of Fluids, 1995, **7**, 1923–1930.

60 A. A. Doinikov, Physical review E, 2001, **64**, 026301.

61 Y. Zhang and S. Li, Ultrasonics Sonochemistry, 2016, **29**, 129–145.

62 Y. Zhang and S. Li, Ultrasonics sonochemistry, 2017, **35**, 431–439.

63 P. L. Marston, The Journal of the Acoustical Society of America, 2019, **146**, EL145–EL150.

64 J. T. Karlsen and H. Bruus, Physical Review E, 2015, **92**, 043010.

65 L. Zhang and P. L. Marston, The Journal of the Acoustical Society of America, 2011, **129**, 1679–1680.

66 T. Schwarz, P. Hahn, G. Petit-Pierre and J. Dual, Microfluidics and Nanofluidics, 2015, **18**, 65–79.

67 A. Garbin, I. Leibacher, P. Hahn, H. Le Ferrand, A. Studart and J. Dual, The Journal of the Acoustical Society of America, 2015, **138**, 2759–2769.

68 S. Lakämper, A. Lamprecht, I. A. Schaap and J. Dual, Lab on a Chip, 2015, **15**, 290–300.

69 A. Lamprecht, S. Lakämper, T. Baasch, I. A. Schaap and J. Dual, Lab on a Chip, 2016, **16**, 2682–2693.

70 G. Thalhammer, C. McDougall, M. P. MacDonald and M. Ritsch-Marte, Lab on a Chip, 2016, **16**, 1523–1532.

71 G. Memoli, C. R. Fury, K. O. Baxter, P. N. Gélat and P. H. Jones, The Journal of the Acoustical Society of America, 2017, **141**, 3364–3378.

72 D. Hartono, Y. Liu, P. L. Tan, X. Y. S. Then, L.-Y. L. Yung and K.-M. Lim, Lab on a Chip, 2011, **11**, 4072–4080.

73 R. Barnkob, P. Augustsson, T. Laurell and H. Bruus, Lab on a Chip, 2010, **10**, 563–570.

74 J. Happel and H. Brenner, Low Reynolds number hydrodynamics: with special applications to particulate media, Springer Science & Business Media, 1983, vol. 1.

75 A. Barani, P. Mosaddegh, S. Haghjooy Javanmard, S. Sepehrirahnama and A. Sanati-Nezhad, Scientific reports, 2021, **11**, 1–17.

76 J. Lei, M. Hill, C. P. de León Albarrán and P. Glynne-Jones, Microfluidics and Nanofluidics, 2018, **22**, 1–14.

77 Tracker, video analysis and modeling tool, `https://physlets.org/tracker/`, [Online; accessed on 05-August-2021].

78 K. Szymczyk, A. Zdziennicka and B. Jańczuk, Journal of solution chemistry, 2018, **47**, 1824–1840.

79 H. Koubali, M. E. Louali, H. Zahir, S. Soufiani, M. Mabrouki and H. Latrache, International Journal of Adhesion and Adhesives, 2021, **104**, 102754.

80 K. Szymczyk, M. Szaniawska and A. Taraba, Colloids and Interfaces, 2018, **2**, 34.

81 D. Saeidi, M. Saghafian, S. Haghjooy Javanmard, B. Hammarström and M. Wiklund, The Journal of the Acoustical Society of America, 2019, **145**, 3311–3319.

82 L. A. Castro and M. Hoyos, Microgravity Science and Technology, 2016, **28**, 11–18.

83 G. T. Silva and H. Bruus, Physical Review E, 2014, **90**, 063007.

84 A. Pavlic, L. Ermanni and J. Dual, Physical Review E, 2022, **105**, L053101.

85 C. Pozrikidis et al., Boundary integral and singularity methods for linearized viscous flow, Cambridge university press, 1992.

86 S. Annamalai, S. Balachandar and M. K. Parmar, Physical Review E, 2014, **89**, 053008.

87 A. Lenshof, C. Magnusson and T. Laurell, Lab on a Chip, 2012, **12**, 1210–1223.